JOURNAL OF COMPUTATIONAL PHYSICS 115, 121–146 (1994)

Generalized Stokes Eigenfunctions: A New Trial Basis for the Solution of Incompressible Navier–Stokes Equations

PAUL F. BATCHO

Program in Applied and Computational Mathematics, Princeton University, Princeton, New Jersey 08544

AND

GEORGE EM KARNIADAKIS*

Center for Fluid Mechanics, Division of Applied Mathematics, Brown University, Providence, Rhode Island 02912

Received October 19, 1993; revised April 4, 1994

The present study focuses on the solution of the *incompressible* Navier–Stokes equations in general, non-separable domains, and employs a Galerkin projection of divergence-free vector functions as a trial basis. This basis is obtained from the solution of a generalized constrained Stokes eigen-problem in the domain of interest. Faster convergence can be achieved by constructing a *singular* Stokes eigen-problem in which the Stokes operator is modified to include a variable coefficient which vanishes at the domain boundaries. The convergence properties of such functions are advantageous in a least squares sense and are shown to produce significantly better approximations to the solution of the Navier–Stokes equations in post-critical states where unsteadiness characterizes the flowfield. Solutions for the eigen-systems are efficiently accomplished using a combined Lanczos–Uzawa algorithm and spectral element discretizations. Results are presented for different simulations using these global spectral trial basis on non-separable and multiply-connected domains. It is confirmed that faster convergence is obtained using the singular eigen-expansions in approximating stationary Navier–Stokes solutions in general domains. It is also shown that 100-mode expansions of time-dependent solutions based on the singular Stokes eigenfunctions are sufficient to accurately predict the dynamics of flows in such domains, including Hopf bifurcations, intermittency, and details of flow structures.

1. INTRODUCTION

The computational requirements to obtain numerical solutions of the Navier–Stokes equations are well documented and are based either on physical scaling arguments [1] or on more rigorous mathematical analysis [2, 3]. Difficulties arise as the Reynolds number or the geometric complexity increases and the required computer speed and memory greatly exceed the current parallel supercomputing capabilities. While the prospect of Teraflop processing power within the next few years is a promising one, it has become clear that simultaneous advances in algorithms are necessary to break what has been characterized as "deadlock" in simulating turbulence in a realistic range of Reynolds number and geometry [1]. The development of a new numerical method for the incompressible Navier–Stokes equations is the objective of this work. It is based on new extensions to existing spectral methods and exploits the modern computational capabilities available today.

There is currently a broad consensus that high-order methods are better suited for direct numerical simulation of turbulence as they typically require a smaller number of grid points for a given amount of scaling information as compared to low-order methods, and correspondingly, in high-accuracy simulations both computing as well as memory cost are significantly lower. This view is exemplified by the use of global spectral methods over the last two decades almost exclusively in simulations of transition and turbulence [4, 5]. The use of spectral methods also allows the incorporation of recent concepts developed in dynamical systems theory, [6], into modern numerical methods.

Work on spectral methods for the solution of the Navier–Stokes equations has been concentrated around approximations based on Fourier expansions or eigenfunctions of a one-dimensional singular Sturm–Liouville operator [7]. These methods rely on the geometric separability and the construction of tensor product representations in multi-dimensional domains. In non-separable or multiply-connected domains the use of domain decomposition has resulted in the construction of spectral element methods [8–11] to handle geometric complexity; these methods still employ tensor product representations within each subdomain.

* Author to whom all correspondence should be addressed.

0021-9991/94 $6.00

The current study focuses on the construction of a global basis set which is geometry-fitted to a given complex geometry domain and exhibits fast convergence rates as in spectral methods. To achieve this, the present study considers an extension of singular Sturm–Liouville theory to multi-dimensions and complex geometry domains. Since solutions of the incompressible Navier–Stokes equations are sought, the basis set must be complete in a Solobev space of divergence-free vector functions. In this study, the basis set is derived from a linear self-adjoint system of partial differential equations coupled by a divergence-free constraint, the generalized Stokes eigen-system [12]. The solenoidal character of the eigenfunctions is advantageous in solving the Navier–Stokes equations via Galerkin projections since incompressibility is automatically satisfied by the expansion and therefore there is no need to solve a pressure equation separately. The latter represents typically a large part of the computation in simulations of incompressible flows [13].

Methodologies of this nature have been implemented by expansions in terms of empirical eigenfunctions (proper orthogonal decomposition, POD, method) [14, 15] and with one-dimensional eigenfunctions based on Jacobi polynomials, [16], for simple geometries. The empirical eigenfunctions are truly multi-dimensional, divergence-free, and geometry-fitted, similar to the properties of the eigenfunction sought in this study. They are also optimal in the L^2 averaged context with respect to the solutions of the governing equations. However, their derivation is based on a decomposition which requires a priori knowledge of the flowfield solution and thus POD methods cannot be used as truly predictive tools.

The eigenfunctions derived in this work are solutions of the generalized Stokes operator in a given computational domain. Their completeness and orthogonality is guaranteed since they are solutions of a linear self-adjoint system of partial differential equations. Two sets of eigenfunctions are considered in this work: First, eigenfunctions of the linear term of the Navier–Stokes equations, the Stokes eigenfunctions, are derived and evaluated for their ability to solve the Navier–Stokes equations. Their convergence properties are studied in the least squares sense when used in N-dimensional series expansions. It is shown that when used to solve the Navier–Stokes equations their convergence rate is bounded by $O(N^{-4/D})$ in a D-dimensional space $\mathfrak{R}^D$. It is also shown that the Stokes eigenfunctions can yield less than 0.1% error when less than 100 eigenfunctions are employed to solve the Stokes equations. However, substantial errors result when solving the Navier–Stokes equations, especially in the high Reynolds number regime. Second, eigenfunctions of the singular Stokes operator are derived. In this case, the Stokes eigen-problem is modified to include a variable coefficient in the Laplacian operator, which vanishes at the boundaries and produces eigenfunctions that could yield exponential convergence rates in approximations of smooth solutions. This formulation leads to better approximations to the solutions of the Navier–Stokes equations for stationary as well as unsteady solutions when compared to the regular Stokes eigenfunctions.

The paper is organized as follows: The formulation and analysis of the generalized Stokes operator is presented in Section 2, along with a presentation of the numerical methods used to solve the eigen-system. The method of inverse orthogonal iteration is used and is found to yield accurate results for a block of the lowest eigenpairs. However, the convergence of this approach is acceptable only if a handful of eigenfunctions are needed. A Lanczos iteration procedure is also implemented, which for large subspaces was found to be the most effective procedure. The discretization of the differential operators is performed by the spectral element method while the imposition of the incompressibility constraint is imposed by a modified Uzawa scheme [17]. The inversion of the matrices, typically of dimension of several thousands, is performed by a mixed preconditioned conjugate gradient/static condensation technique. In Section 3, the Stokes eigen-system is examined in more detail and results are presented for the various geometries studied. In Section 4, a singular Stokes eigen-system is examined. The construction and convergence properties of the singular operator are discussed and results are presented for the various domains and operators considered. In Section 5 the computational complexity of obtaining several hundred eigenfunctions is analyzed. In Section 6, the Stokes and singular Stokes eigen-systems are used in a least squares projection of solutions of the Navier–Stokes equations. In Section 7, Galerkin projections of the Navier–Stokes equations are presented for stationary and time dependent solutions. The eigen-expansions are examined for their ability to solve the Navier–Stokes equations with $O(10^2)$ eigenfunctions. Finally, a summary of the work and a discussion of future developments of the proposed method are addressed in Section 8.

2. CONSTRAINED GENERALIZED EIGEN-SYSTEM

2.1. Formulation

The present study focuses on the solution of the *incompressible* Navier–Stokes equations in general, non-separable domains and employs a Galerkin projection of divergence-free vector functions as a trial basis. This basis is obtained from the solution of the following generalized constrained self-adjoint eigen-problem (EP):

$$-\nabla \Pi + \nabla \cdot [\rho(\mathbf{x}) \nabla \mathbf{w}] + q(\mathbf{x})\mathbf{w} = \lambda \mathbf{w} \qquad \text{in } \Omega \qquad (1a)$$

$$\nabla \cdot \mathbf{w} = 0 \qquad \text{in } \Omega \qquad (1b)$$

$$\mathscr{B}\mathbf{w} = 0 \qquad \text{on } \partial\Omega, \qquad (1c)$$

where $\mathbf{w} \in H_0^1$ is a global spectral basis, H_0^1 is a Sobolev space of divergence-free vector functions, $\mathscr{B}$ is a linear boundary operator, and $\rho(\mathbf{x}) > 0$ in the interior of the domain Ω; $\rho(\mathbf{x}) \in C^1$ and may vanish on the domain boundary $\partial\Omega$. The boundary operator $\mathscr{B}$ can, in general, enforce any boundary condition suitable for eigenproblems: homogeneous Robin, Neumann, Dirichlet, periodic, or mixed. This study focuses on the mixed Dirichlet and periodic cases since these boundary conditions lead to the elimination of the pressure gradient of the Navier–Stokes equations when divergence-free projections are performed onto them. The scalar $\Pi(\mathbf{x})$ is an auxiliary quantity used to impose the solenoidal constraint, Eq. (1b). The above eigen-system is referred to as a generalized Stokes system because in the case where [$\rho(\mathbf{x}) = 1$, and $q(\mathbf{x}) = 0$] it reduces to the Stokes eigen-system.

The main results of Sturm–Liouville theory ($q(\mathbf{x}) < 0$) for ordinary differential equations, [18–20], carry over to the above system since the coupling is only present through the scalar function $\Pi(\mathbf{x})$. Theoretical studies on the spectrum of this class of operators have been carried out by Mètivier [21]. The completeness and orthogonality of the eigenfunctions are guaranteed through the self-adjointness of the operator and boundary conditions. Constantin and Foias [22] give a thorough discussion of the Stokes system and present proofs on regularity and completeness. The theory of single symmetric differential operators given by the form of (1a) is discussed in detail in Gårding [23] and Strauss [24].

In this work we seek numerical solutions of EP in general complex computational domains with a high degree of accuracy. To obtain accurate solutions we will use a high-order spatial discretization method along with an appropriate technique to enforce the divergence-free constraint, Eq. (1b). More specifically a spectral element discretization in space, (Patera [8], Maday and Patera [25]), along with the modified Uzawa algorithm, Rønquist [17], is used. Finally, an efficient eigen-solver must be used to obtain a specified subspace of the leading several hundred eigensolutions.

2.2. Numerical Methods

Consider a domain discretized into general quadrilateral spectral elements, as shown in (Fig. 1). The corresponding variational formulation of EP can be written in the general algebraic form

$$-H\mathbf{w}_i + D_i^{\mathrm{T}}\Pi = B\lambda\mathbf{w}_i, \qquad i = 1, \ldots, d \qquad \text{in } \Omega \quad (2a)$$

$$-D_i\mathbf{w}_i = 0 \qquad \text{in } \Omega. \quad (2b)$$

Here H is the discrete analog of the operator $\nabla \cdot [\rho(\mathbf{x})\nabla] + q(\mathbf{x})$ and is symmetric positive definite, matrix B is the mass matrix, and D^{T} is the transpose of the discrete gradient operator. Next, we apply a variant of the Uzawa algorithm, [17], as

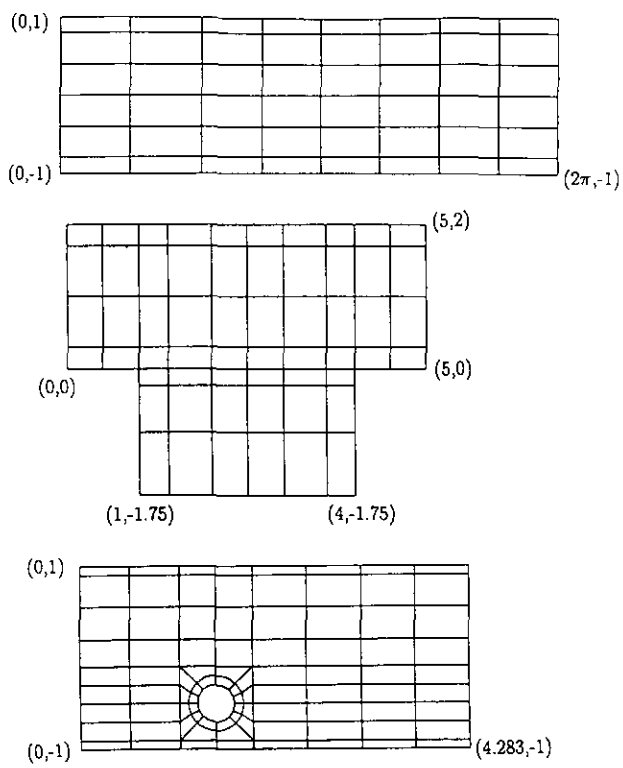

FIG. 1. Spectral element skeleton meshes for the three domains studied: (a) channel domain consisting of 48 spectral elements; (b) grooved channel domain consisting of 58 spectral elements; (c) eddy-promoter domain consisting of 88 spectral elements. Periodic boundary conditions are imposed in the streamwise x-direction.

$$-S\Pi = -D_i H^{-1} B\lambda\mathbf{w}_i, \quad (3a)$$

$$-H\mathbf{w}_i = B\lambda\mathbf{w}_i - D_i^{\mathrm{T}}\Pi, \qquad i = 1, \ldots, d, \quad (3b)$$

where $S \equiv D_i H^{-1} D_i^{\mathrm{T}}$ and is a positive semi-definite matrix. In the case of the Stokes system the matrix S is well conditioned due to the product of the two first-order gradient operators "divided" by the second-order Laplacian. The embedded H^{-1} makes S full and therefore an iterative method is employed for its inversion. The pressure field is solved for by a nested global inner static condensation/outer conjugate gradient method. The corresponding matrix of the Helmholtz operator H is inverted by a direct solver using static condensation. The pressure field is solved on a Gauss Legendre mesh of order $N-2$ while the velocity fields are solved on a Gauss–Lobatto Legendre mesh of order N. The use of the two meshes deals effectively with the problem of spurious pressure modes [26]. The use of the outer conjugate solver on the pressure allows the divergence of the velocity field to be directly enforced on the Gauss Legendre mesh by the residual of the iterative solver.

However, the level of divergence of the velocity field on the Gauss–Lobatto Legendre mesh is subject to the discretization error and not simply the residual of the pressure inversion. For non-smooth domains the accuracy of the solution could be degraded and lead to non-negligible divergence errors. These issues will be addressed in a later section.

To see more clearly that this formulation leads to a generalized eigen-problem, system (3) is recast in the following block matrix form for a two-dimensional case as

$$\begin{bmatrix} -H & 0 \\ 0 & -H \end{bmatrix}\begin{bmatrix} \mathbf{w}_1 \\ \mathbf{w}_2 \end{bmatrix}=\begin{bmatrix} B-S_{11} & -S_{12} \\ -S_{21} & B-S_{22} \end{bmatrix}\begin{bmatrix} \lambda\mathbf{w}_1 \\ \lambda\mathbf{w}_2 \end{bmatrix},$$

where

$$S_{ij}\equiv D_i^{\mathrm{T}} S^{-1} D_j H^{-1} B, \qquad i=1,2, \quad j=1,2. \tag{4}$$

In this form, it can be seen that the pressure acts to decouple the system and impose the incompressibility constraint. The obtained eigenfunctions are orthogonal with respect to the mass matrix B. Similar systems resulting from finite element discretizations were treated in the work of Cliffe *et al.* [27].

2.2.1. *Inverse Orthogonal Iteration–Uzawa Method*

Here the above block system is rewritten in an iterative form that is appropriate for the inverse power method, i.e.,

$$\begin{bmatrix} -H & 0 \\ 0 & -H \end{bmatrix}\begin{bmatrix} \mathbf{w}_1^{m+1} \\ \mathbf{w}_2^{m+1} \end{bmatrix}=\begin{bmatrix} B-S_{11} & -S_{12} \\ -S_{21} & B-S_{22} \end{bmatrix}\begin{bmatrix} \hat{\mathbf{w}}_1^{m} \\ \hat{\mathbf{w}}_2^{m} \end{bmatrix} \equiv \tilde{B}\begin{bmatrix} \hat{\mathbf{w}}_1^{m} \\ \mathbf{w}_2^{m} \end{bmatrix},$$

where m is the iteration number and $\hat{\mathbf{w}}$ is a normalized velocity $\mathbf{w}^m/\|\mathbf{w}^m\|$. The above system is solved by premultiplying the $\tilde{B}^{-1}$ and thus preserving the self-adjointness of the system and orthogonality of the eigenfunctions with respect to the mass matrix B. We obtain

$$\tilde{H}\mathbf{w}^{m+1}\equiv[\tilde{B}^{-1}]\begin{bmatrix} -H & 0 \\ 0 & -H \end{bmatrix}\mathbf{w}^{m+1}=\hat{\mathbf{w}}^m.$$

The generalized eigen-problem is thus reduced to the standard form and, as will be shown below, no additional inversions are needed. The inverse orthogonal iteration algorithm can now be presented. In standard form we have

$$\tilde{H}\mathbf{Z}^m=\mathbf{Q}^m$$
$$\mathbf{Z}^m=\mathbf{Q}^{m+1}R,$$

where capital bold-faced letters indicate matices whose columns are filled with the vector functions of the p-subspace, e.g., $\mathbf{Q}=[\mathbf{q}_1,\mathbf{q}_2,\ldots,\mathbf{q}_p]$. The vector function QR decomposition on the $n\times p$ matrix $\mathbf{Z}^m$ was performed by a modified Gram–Schmidt procedure.

In decoupled form we solve for $\mathbf{z}_i^m$ as follows.

ALGORITHM A.

$$S\phi^m=D_iH^{-1}B\mathbf{q}_i^m$$
$$-H\mathbf{z}_i^m=-D_i^{\mathrm{T}}\phi^m+B\mathbf{q}_i^m$$
$$\mathbf{Z}^m=\mathbf{Q}^{m+1}R, \qquad m=1,2,3,\ldots,$$

where, initially, $\mathbf{q}_i^0=\hat{\mathbf{w}}_i^0$. Here bold-faced symbols indicate vector functions and subscript i represents the component of the vector function.

2.2.2. *Lanczos–Uzawa Method*

The rate of convergence to a p-subspace of the eigen-system can be enhanced by using the Lanczos iteration method [28]. Rapid convergence is obtained for the first few eigensolutions if the inverse of the matrix is employed in the three term recurrence relation, i.e.,

$$\mathbf{q}_{j+1}\beta_j=\tilde{H}^{-1}\mathbf{q}_j-\mathbf{q}_j\alpha_j-\mathbf{q}_{j-1}\beta_{j-1}, \tag{5}$$

where $\tilde{H}$ was defined above. Given a $\mathbf{q}_j$ from the previous iteration we evaluate the matrix-vector product by solving for $\mathbf{u}_j$ from $\tilde{H}\mathbf{u}_j=\mathbf{q}_j$. The inversion is carried out in the same fashion as described for the inverse iteration, Algorithm A above. Complete re-orthogonalization is performed at each iteration j; the algorithm is presented below:

ALGORITHM B.

$$\mathbf{q}_j=\mathbf{r}_{j-1}/\beta_{j-1}$$
$$\mathbf{u}_j=\tilde{H}^{-1}\mathbf{q}_j$$
$$\mathbf{r}_j=\mathbf{u}_j-\mathbf{q}_{j-1}\beta_{j-1}$$
$$\alpha_j=\mathbf{q}_j^{\mathrm{T}}B\mathbf{r}_j$$
$$\mathbf{r}_j=\mathbf{r}_j-\mathbf{q}_j\alpha_j$$
$$\mathbf{r}_j=\mathbf{r}_j-\mathbf{q}_k(\mathbf{q}_k^{\mathrm{T}}B\mathbf{r}_j), \qquad k=j,j-1,\ldots,2,1,$$
$$\beta_j=(\mathbf{r}_j^{\mathrm{T}}B\mathbf{r}_j)^{1/2}$$

where $\mathbf{r}_0$ is an initial guess and $\beta_0=(\mathbf{r}_0^{\mathrm{T}}B\mathbf{r}_0)^{1/2}$.

3. EIGENFUNCTIONS OF THE STOKES SYSTEM

The Stokes eigenfunctions have been used in several mathematical studies of the Navier–Stokes equations (Foias *et al.* [29], Constantin *et al.* [2], and Foias *et al.* [30]). The Stokes eigen-system is defined by the generalized

Stokes system where $p(\mathbf{x}) = 1$ and $q(\mathbf{x}) = 0$. Therefore EP is reduced to

$$-\nabla \Pi + \nabla^2 \mathbf{w} = \lambda \mathbf{w} \quad \text{in } \Omega \tag{6a}$$

$$\nabla \cdot \mathbf{w} = 0 \quad \text{in } \Omega \tag{6b}$$

$$\mathscr{B}\mathbf{w} = 0 \quad \text{on } \partial\Omega. \tag{6c}$$

It can be seen that the operator is self-adjoint and that homogeneous or periodic boundary conditions will yield a fully self-adjoint problem [22]. The function being approximated is assumed to be square integrable, solenoidal, and either homogeneous or periodic at the boundary. It can therefore be approximated by a series expansion of the Stokes eigenfunctions

$$\mathbf{u} = \sum_{i=0}^{N} a_i \mathbf{w}_i, \tag{7}$$

where the series is expanded in a hierarchy with respect to the eigenvalues λ_i, where λ_0 is the smallest eigenvalue, and the coefficients are obtained from

$$a_i = (\mathbf{w}_i, \mathbf{u}) \equiv \int_\Omega \mathbf{w}_i \cdot \mathbf{u}\, d\mathbf{x}. \tag{8}$$

Substituting Eq. (6a) into (8) and integrating by parts four times (noting that the scalar $\Pi(\mathbf{x})$ drops out due to Green's identity and that the eigenfunctions are homogeneous or periodic), we arrive at

$$a_i = -\frac{1}{\lambda_i^2}\left[(\mathbf{w}_i, \nabla^4 \mathbf{u}) - \oint [\nabla^2 \mathbf{u} \cdot (\mathbf{n} \cdot \nabla \mathbf{w}_i)]\, ds\right]. \tag{9}$$

In order to achieve convergence rates higher than $O(1/\lambda_i^2)$ the boundary term in Eq. (9) must vanish and therefore the Laplacian of the velocity field must go to zero on the domain boundary $\partial\Omega$. By examining the Navier–Stokes equations we find that for a nonzero flow around a surface the Laplacian cannot vanish on the surface and therefore the surface integral will not vanish. In the special case of periodic boundary conditions in every direction exponential convergence can, of course, be recovered. Thus, for non-periodic domains the best rate of convergence that can be obtained, in the L^2 least squares context, is given by $O(1/\lambda_i^2)$. Given the estimate on the scaling of the spectrum as $\lambda_n \sim O(n^{2/D})$ in a D-dimensional space $\Re^D$, [22], an upper bound for the convergence rate for the Stokes eigenfunction expansion is

$$O(n^{-4/D}). \tag{10}$$

In two dimensions ($D = 2$) the upper bound for the convergence rates of the velocity field is given by $a_n \sim O(n^{-2})$ and shows quadratic convergence.

3.1. Analytical and Computational Results

3.1.1. *Separable Domains*

The eigenfunctions of the Stokes operator can be solved analytically for simple separable domains by a scalar and vector potential decompositon as presented in Salwen *et al.* [31]. Here the solution for a 2D plane channel domain with one periodic direction, (Fig. 1a), is briefly summarized.

For even solutions of streamwise (x-direction) velocity in the y-direction,

$$u = \left(-\frac{\cos(\sigma y)}{\cos \sigma} + \frac{\cosh(\alpha y)}{\cosh \alpha}\right) e^{i\alpha x} \tag{11a}$$

$$v = \left(\frac{\alpha}{\sigma}\frac{\sin(\sigma y)}{\cos \sigma} - \frac{\sinh(\alpha y)}{\cosh \alpha}\right) e^{i\alpha x} \tag{11b}$$

where $\mathbf{w} = (u, v)$, α is the wave number in the x-direction, and the eigenvalues are obtained from the relation

$$\sigma \coth(\sigma) = \alpha \coth(\alpha) \tag{11c}$$

where

$$\sigma^2 = -\lambda - \alpha^2. \tag{11d}$$

For $\alpha = 0$ the eigenvalues are given by

$$\lambda = \left(\frac{2m+1}{2}\pi\right)^2, \qquad m = 0, 1, 2, 3, \ldots. \tag{11e}$$

For odd solutions of streamwise velocity in the y-direction,

$$u = \left(-\frac{\sin(\sigma y)}{\sin \sigma} + \frac{\sinh(\alpha y)}{\sinh \alpha}\right) e^{i\alpha x} \tag{12a}$$

$$v = \left(-\frac{\alpha}{\sigma}\frac{\cos(\sigma y)}{\sin \sigma} - \frac{\cosh(\alpha y)}{\sinh \alpha}\right) e^{i\alpha x}, \tag{12b}$$

and the eigenvalues are obtained from the relation

$$\alpha \tan(\sigma) = -\sigma \tanh(\alpha). \tag{12c}$$

For $\alpha = 0$ the eigenvalues are given by

$$\lambda = (m\pi)^2, \qquad m = 1, 2, 3, \ldots. \tag{12d}$$

Noting the dependence of the eigenfunctions on λ the convergence rate estimates given in Section 3.1 can be adjusted for the channel domain. For least squares projections of solenoidal velocity fields we obtain $a_n \sim O(n^{-3/2})$.

TABLE I

Eigenvalues of the Channel Domain (Fig. 1a)

i	λ_i computed	Residual
1	2.467401100272	4.05×10^{-10}
2	9.313740164676	9.43×10^{-10}
3	9.313740164690	9.76×10^{-10}
4	9.869604401090	9.28×10^{-7}

TABLE II

Eigenvalues of the Grooved Channel Domain (Fig. 1b)

i	λ_i computed	Residual
1	2.1378710	2.48×10^{-5}
2	4.5282150	1.33×10^{-4}
3	6.9162780	3.23×10^{-4}
4	7.5417144	1.59×10^{-4}

Computations have been performed for the four leading eigensolutions for the channel domain using the inverse orthogonal iteration–Uzawa algorithm. The computational mesh for the spectral element discretization is shown in Fig. (1a); an eleventh-order polynomial was used on the Gauss–Lobatto mesh for both the x- and y-directions for each element in the spectral element discretization. The channel results are shown in Table I, where the residual is defined as the L^2 norm of Eq. (6a) and reflects the level of the divergence of the solution. The first ($m = 0$) eigenvalue has an exact solution of $\pi^2/4$ and the computed value differs by $O(10^{-10})$; the fourth eigenvalue differs from the exact solution, π^2, by $O(10^{-7})$. The loss of accuracy of the fourth eigenvalue is due to the nonzero auxiliary scalar $\Pi(\mathbf{x})$ of modes two and three and their induced errors. The parallel flow modes all have exact solutions where the auxiliary scalar $\Pi(\mathbf{x})$ is identically zero. The second and third modes correspond to the real and imaginary part of a single wave in the x-direction, $f(y)\, e^{i\alpha x}$ and have the same eigenvalue; the third has a phase shift of $\pi/2$ in the x-direction relative to the second. The computation indicates a difference between the second and third eigenvalue in the eleventh decimal place.

3.1.2. *Complex Domains*

The grooved channel domain shown in Fig. 1b is considered first. Computations have been performed for the four leading eigensolutions using the inverse orthogonal iteration–Uzawa algorithm. The computational mesh for the spectral element discretization is given in Fig. 1b; an eleventh-order polynomial was used on the Gauss–Lobatto mesh for both the x- and y-directions for each spectral element. The leading four eigenvalues for the grooved channel domain are given in Table II and the corresponding vector

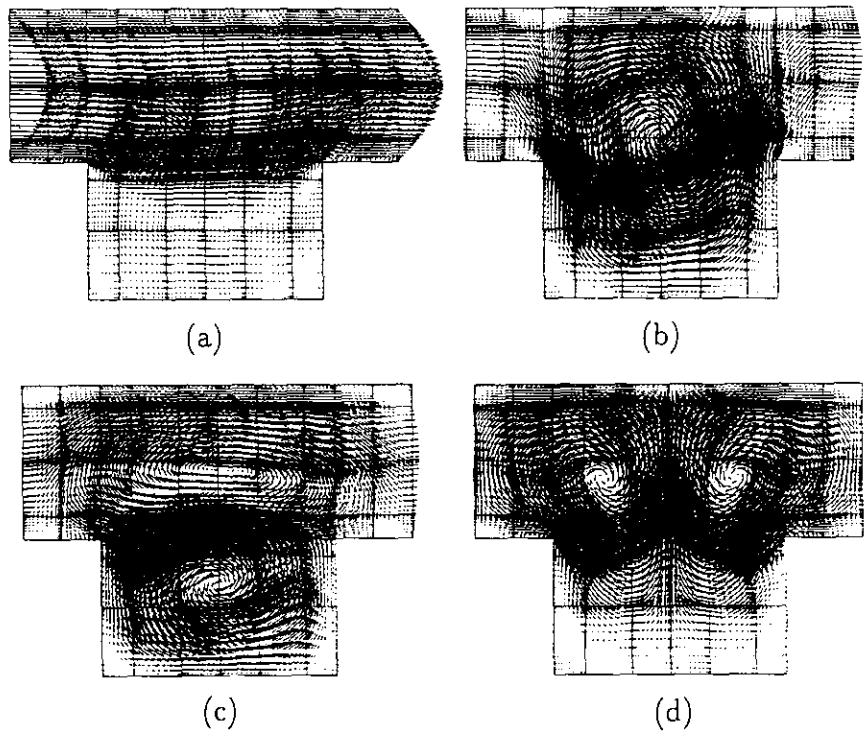

FIG. 2. Velocity vector plots of the first four Stokes eigenfunctions for the grooved channel domain. A 13th-order Gauss Lobatto–Legendre polynomial was used in the spectral element discretization in both spatial directions. The first, second, third, and fourth eigenfunctions are plotted in (a), (b), (c), and (d), respectively.

eigenfunctions are plotted in Fig. 2. The residual is defined as the L^2 norm of Eq. (6a) and reflects the level of the divergence of the solution. The geometric singularities of the grooved channel domain prevent the solution accuracy from reaching arbitrarily small levels.

The Lanczos–Uzawa algorithm was also used to converge the first one hundred eigenvalues to suitable small tolerance levels. The spectrum of the grooved channel domain using a spectral element computation with a 13×13 polynomial in each element is presented in Fig. 3. The change in the eigenvalues from an 11×11 to a 13×13 order polynomial was $O(10^{-4})$, reflecting the level of divergence in the solution. Since the one hundredth eigenfunction was also converged to the same accuracy, with respect to the lower resolution, as the first, it was assumed that the resolution was acceptable for all one hundred modes. The linear distribution of the spectrum is consistent with the scaling estimates presented above. In Fig. 4 representations of the higher vector modes of the Stokes eigen-system for the grooved channel domain are plotted. The divergence level of the eigenfunctions were $O(10^{-3}) - O(10^{-4})$ for all one hundred modes.

Next the computed Stokes eigenfunctions in the multiply

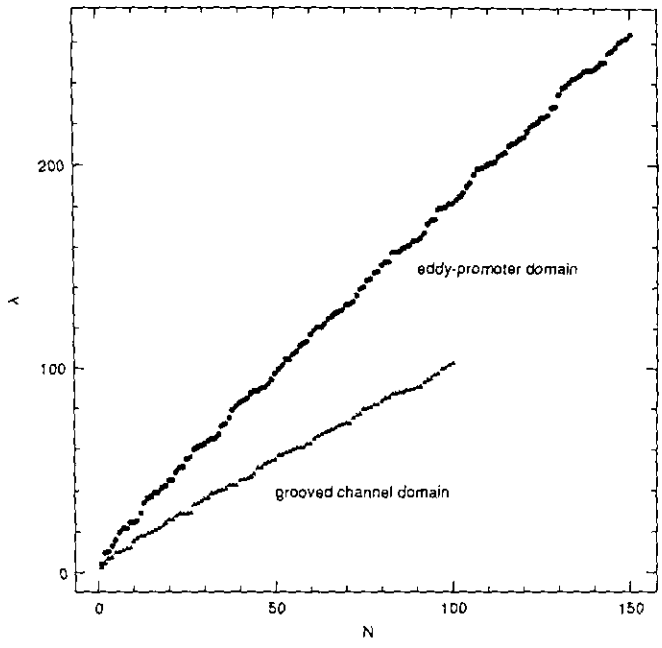

FIG. 3. The leading 100 eigenvalues for the Stokes eigen-system computed in the grooved channel domain and the leading 150 Stokes eigenvalues for the eddy-promoter domain.

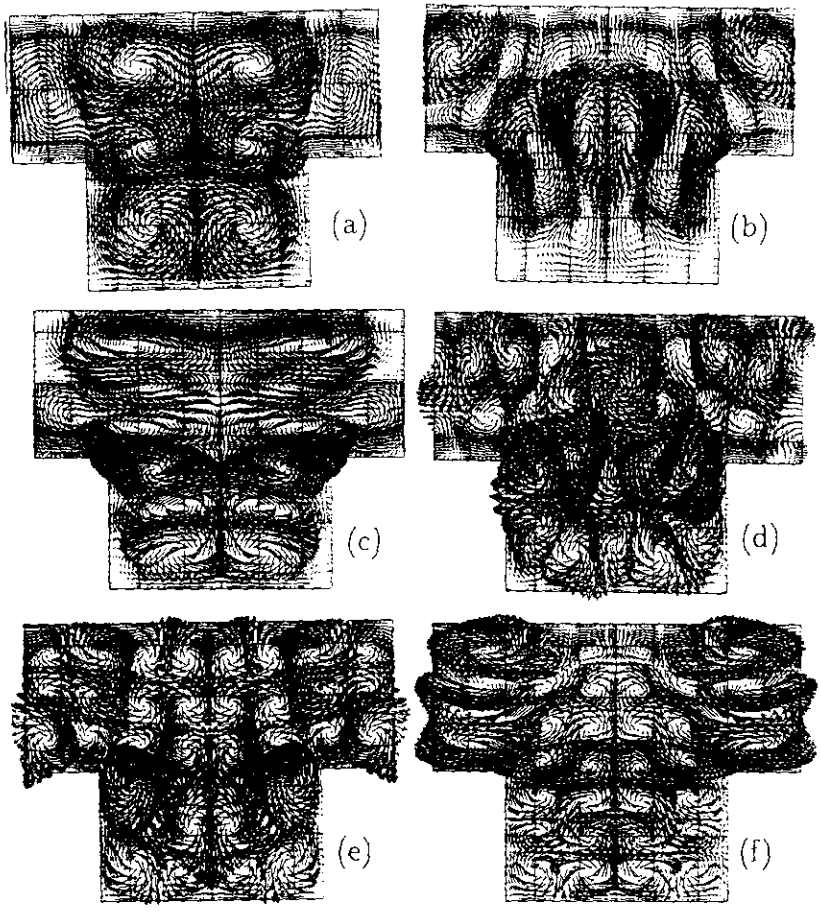

FIG. 4. Velocity vector plots for eigenfunctions 10, 20, 30, 40, 50, and 60 for the Stokes eigen-system in the grooved channel domain are shown in (a)-(f), respectively. A 13th-order Gauss Lobatto-Legendre polynomial was used in the spectral element discretization in both spatial directions.

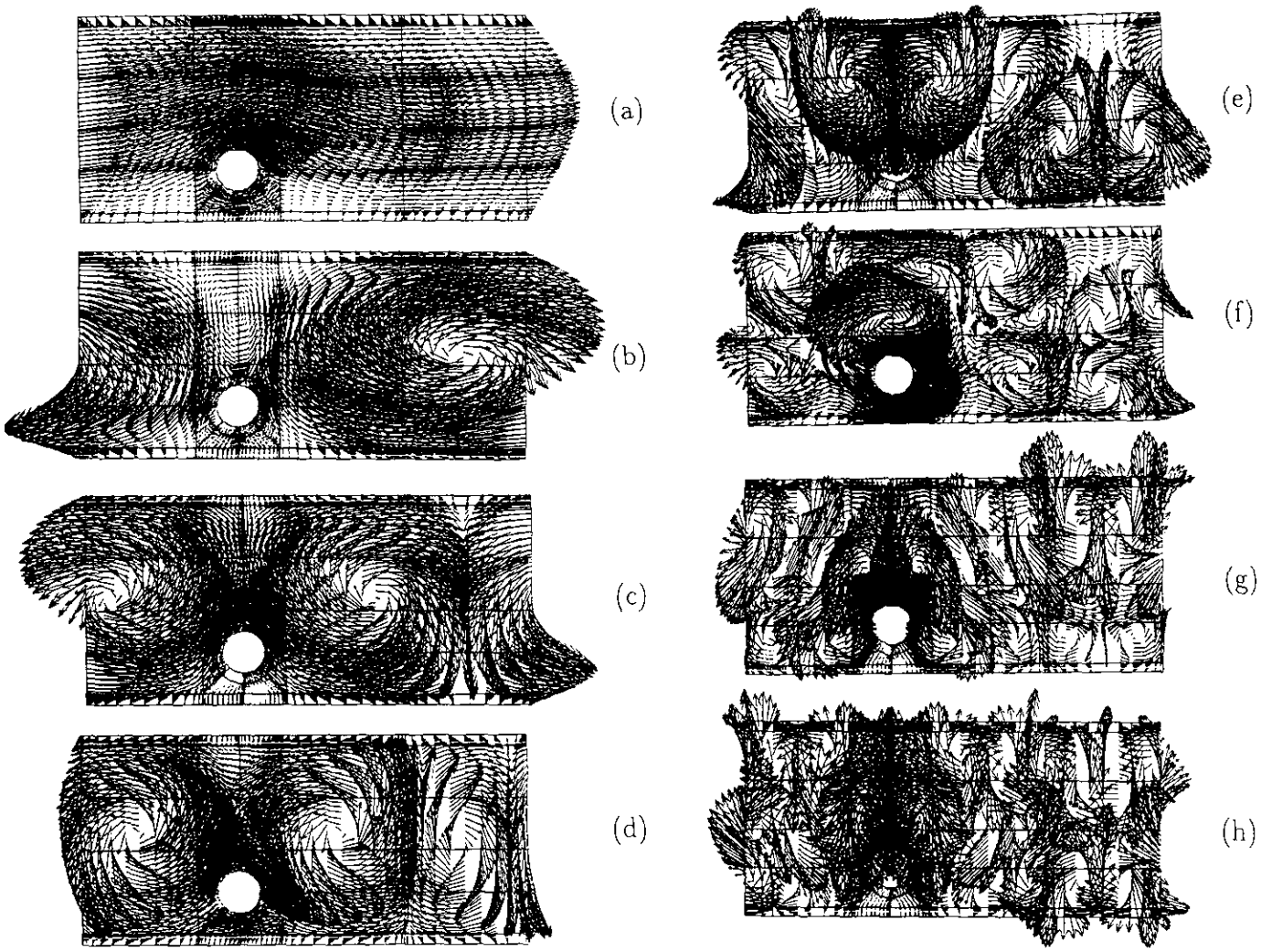

FIG. 5. Velocity vector plots of the first four Stokes eigenfunctions for the eddy-promoter domain. A 13th-order Gauss Lobatto–Legendre polynomial was used in the spectral element discretization in both spatial directions. The first, second, third, and fourth eigenfunctions are plotted in (a)–(d), respectively. Velocity vector plots for eigenfunctions 10, 20, 30, and 40 are plotted in (e)–(h), respectively.

connected eddy-promoter domain (Fig. 1c) are presented. This domain is smooth, $\partial\Omega \in C^{\infty}$, so that arbitrarily small divergence levels may be achieved through the algorithms presented above. In Fig. 3 the associated eigenspectrum and in Fig. 5 a representation of the vector eigenfunctions are presented. These computations were performed with the Lanczos–Uzawa algorithm using a thirteen-order polynomial for both directional components in each of the 54 spectral elements. The divergence level for the first 25 eigenfunctions was $O(10^{-6})$ and then it was gradually degraded to a level of $O(10^{-4})$ for the 60th eigenfunction. This was due to relatively poor resolution of the higher modes. A highly resolved mesh was then used with twice the number of elements in the x- and y-directions. The divergence levels for a 30th-order spectral element simulation on the high resolution 88-element mesh was improved to levels of $O(10^{-7})$ for the 60th eigenfunction. The computed eigenvalues for both domains follow a linear scaling with respect to the index of the eigenvalue and is in agreement with the theoretical estimates presented in Section 3.1.

4. EIGENFUNCTIONS OF THE SINGULAR STOKES SYSTEM

4.1. Convergence Properties

The discussions above have shown that the Stokes eigenfunctions yield less than optimal convergence rates in the context of approximation theory. This problem can be remedied by noting that the Laplacian operator with a variable coefficient vanishing at the boundaries in such a way that

$$0 = \lim_{\varepsilon \to 0} \left[\oint \rho(\mathbf{x}) [\nabla^p \mathbf{u} \cdot (\mathbf{n} \cdot \nabla \mathbf{w}_i)] \, ds \right] \tag{13}$$

(where the limit expresses the value of the integral as the boundary $\partial\Omega$ is approached) will yield eigenfunctions that exhibit exponential convergence rates for smooth functions ($\mathbf{u} \in C^\infty$). For non-smooth vector functions the convergence rates are dictated by the degree of smoothness of the function. Following the analysis given in Section 3.1 we arrive at $a_n \sim O(\lambda_n^{-p})$, where p is the highest derivative for which Eq. (13) holds. The operator from which the eigenfunctions are derived is contained within the class covered by the generalized Stokes system EP. The one-dimensional version of the singular operator has been used in the analysis of spectral polynomial approximations, Gottlieb and Orszag [7]; a recent review on the theory is given by Hajmirzaahmad and Krall [32]. However, there has been no attempt up to this point to study the applicability of the two-dimensional version in complex domains. The lack of analytical tools to deal with such domains is certainly considered to be the main obstacle for such studies. In the case of the constrained EP, exponential convergence can be achieved only if $\Pi(\mathbf{x})$ and its derivatives satisfy special conditions.

4.2. Construction of Singular Systems

Due to the singular nature of the operator, the ability to impose homogeneous Dirichlet boundary conditions is expected to be compromised as in the one-dimensional singular Sturm–Liouville operators [32]. The objective is to construct a system that yields eigenfunctions which are homogeneous at Dirichlet boundaries or have periodic boundary conditions and exhibit exponential convergence rates for smooth solutions. Such a system can be constructed by noting that the diagonal coefficient $q(\mathbf{x})$ can be used to control the limiting behavior of the eigenfunctions near the boundaries. The variational form of the eigenproblem states that $\int_\Omega [q(\mathbf{x})\, \mathbf{w}_i \cdot \mathbf{w}_i]\, d\mathbf{x}$ must remain bounded. One possible construction is to choose $q(\mathbf{x})$ such that $q(\mathbf{x}) \sim 1/\hat{\rho}(\mathbf{x})$ near the boundaries so that the eigenfunctions are forced to approach zero where $\hat{\rho}(\mathbf{x})$ vanishes. The scalar function $\hat{\rho}(\mathbf{x})$ is chosen to be positive definite in the interior of the domain and vanish at the Dirichlet boundaries. The singular Stokes system is therefore defined as

$$-\nabla \Pi + \nabla \cdot [\rho(\mathbf{x})\, \nabla \mathbf{w}] - \frac{\mathbf{w}}{\hat{\rho}(\mathbf{x})} = \lambda \mathbf{w} \qquad \text{in } \Omega \qquad (14a)$$

$$\nabla \cdot \mathbf{w} = 0 \qquad \text{in } \Omega \qquad (14b)$$

$$\mathcal{B}\mathbf{w} = 0 \qquad \text{on } \partial\Omega. \qquad (14c)$$

The choice of $\hat{\rho}(\mathbf{x})$ is a crucial element of this construction. It is required that the rate at which $\hat{\rho}(\mathbf{x}) \to 0$ at the boundary $\partial\Omega$ be sufficiently rapid so that the integrability (in the variational statement) of the diagonal term is dictated by the homogeneity of the eigenfunction $\mathbf{w}$. As a counterexample, the choice for a one-dimensional operator where $\hat{\rho}^{-1}(x) = 1/\sqrt{1-x^2}$ yields the diagonal term integrable without the need for $\mathbf{w}$ to approach zero; in this case $\mathbf{w}$ must only be bounded since $\hat{\rho}^{-1}(x)$ is itself integrable.

The variable coefficients of the singular Stokes system must be readily determined in general complex geometries and $\nabla\rho(\mathbf{x})$ must be square integrable. A suitable source for the coefficients is to determine them as solutions of second-order elliptic partial differential equations. The positive definiteness of the scalar $\rho(\mathbf{x})$ can be guaranteed by the minimum principle property of elliptic operators; in addition, the operators can be easily inverted by standard techniques. The Poisson equation with a negative definite (constant) forcing is one possible choice,

$$\nabla^2 \rho(\mathbf{x}) = C < 0 \qquad \text{in } \Omega \qquad (15a)$$

$$\mathcal{B}\rho(\mathbf{x}) = 0 \qquad \text{on } \partial\Omega. \qquad (15b)$$

For the domains studied in Fig. 1, $\rho(\mathbf{x}) \in C^\infty$, for the channel and eddy-promoter domains, (1a) and (1b), and $\rho(\mathbf{x}) \in C^1$ for the grooved channel domain, (1b). In this study the choice of $q(\mathbf{x}) = -4/\rho(\mathbf{x})$ is examined for various L^∞ norms of $\rho(\mathbf{x})$ defined from Eq. (15a), where C is a constant. The computed scalar functions, $\rho(\mathbf{x})$, for the grooved channel and eddy-promoter domains are plotted in Fig. 6.

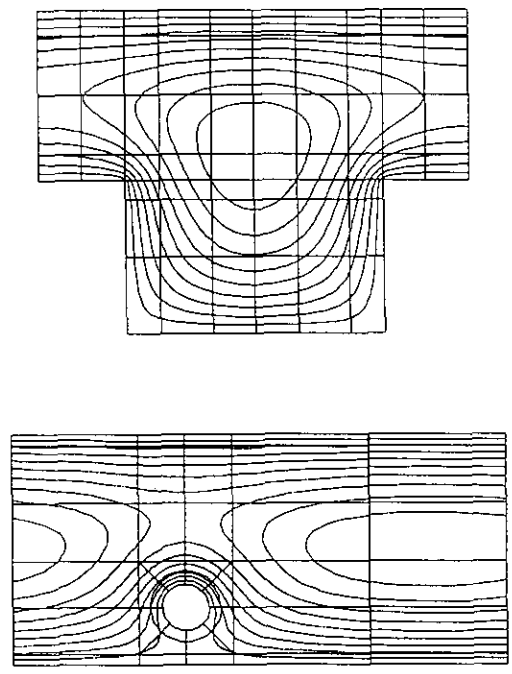

FIG. 6. The computed scalar function $\rho(\mathbf{x})$ for the grooved channel and eddy-promoter domains. The solution of a Poisson equation subject to a constant negative forcing was used to generate $\rho(\mathbf{x})$. The computation is based on a spectral element discretization using a 13th-order Gauss Lobatto–Legendre polynomial in both spatial directions.

In the case of the channel domain this system reduces to the associated Legendre functions, [18], for $\rho(y) = 1 - y^2$ for $y \in [-1, 1]$; i.e.,

$$(\rho(y)\, P'_{n,h})' - \frac{h^2 P_{n,h}}{\rho(y)} + \lambda_n P_{n,h} = 0, \qquad (16a)$$

where

$$P_{n,h} = \rho(y)^{h/2} \frac{d^h P_n}{dy^h}, \qquad h = 1, 2, 3, \ldots. \qquad (16b)$$

A proof of the existence and regularity of a complete set of homogeneous eigenfunctions for the singular Stokes system is not presented here. However, the construction suggested here is supported by the one-dimensional analog of singular second-order operators (e.g., Sturm–Liouville).

4.3. Computational Results

4.3.1. *Separable Domains*

For the channel flow domain the natural choice for the scalar $\rho(\mathbf{x})$ is $1 - y^2$ (noting that $q(\mathbf{x}) = -4/\rho(\mathbf{x})$). For the channel domain the first eigenfunction in the singular Stokes eigen-system is a parabola and the set of parallel flow modes are the associated Legendre functions of order two, $h = 2$ and $\|\rho(\mathbf{x})\|_\infty = 1.0$. The first eigenfunction is the exact solution for stationary (laminar) flows, as compared to the Stokes eigensystem where the first eigenfunction is a cosine profile. The singular operator yields possible advantages over the Stokes eigen-system since the eigenfunctions appear to resemble the solution of the Navier–Stokes equations more closely in the wall region. The first few modes look qualitatively similar to the Stokes eigenfunctions as would be expected since they both must satisfy the same hierarchy of scale information that forms a complete set. The leading eigenfunction is computed to within an L^∞ error norm of 10^{-8} for the given computational resolution (as in Section 3.2.1); see [12] for more details.

4.3.2. *Complex Domains*

The scalar function $\rho(\mathbf{x})$, shown in Fig. 6 and computed from Eq. (15a) is used for the solution of a singular Stokes eigen-system in the grooved channel domain. The eigenvalue spectra for the leading 100 modes with the $\|\rho(\mathbf{x})\|_\infty = 1.0$, 1.5, and 2.0 are presented in Fig. 7, along with the Stokes spectrum. In Fig. 8 the velocity vector plots for the four leading modes and selected higher eigenfunctions for the grooved channel domain are presented. The modes were computed using the Lanczos–Uzawa method

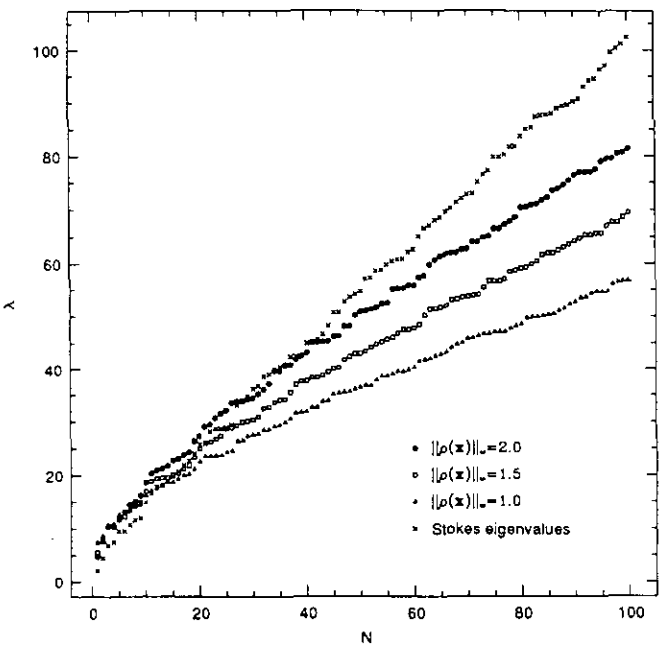

FIG. 7. The leading 100 eigenvalues for the singular Stokes eigen-system are plotted for the grooved channel domain. The different points correspond to $\|\rho(\mathbf{x})\|_\infty = 1.0$, 1.5, and 2.0. The spectrum for the Stokes eigen-system is also included for comparison.

with a $\|\rho(\mathbf{x})\|_\infty = 1.5$. The $\|\rho(\mathbf{x})\|_\infty = 1.5$ condition was chosen since it gave a first mode that is nearly optimal for the Stokes flow in an L^2 context with respect to the $\|\rho(\mathbf{x})\|_\infty$ parameter. The divergence level for the computed eigenfunctions were $O(10^{-2} - 10^{-3})$, roughly an order of magnitude larger than the Stokes eigen-system. The eigenvalue spectrum for the leading 150 modes for the eddy-promoter domain are shown in Fig. 9.

For both the grooved channel and eddy-promoter domains the qualitative features of the leading modes resemble the Stokes eigen-system with regard to the hierarchy of scaling information. The higher modes begin to deviate from the Stokes eigen-system not by the number of zeros but rather in their distribution. The singular property of the operator tends to cluster zeros of the eigenfunctions closer to the boundaries in the same way as one-dimensional singular Sturm–Liouville polynomials do.

The computations presented above were performed using the Lanczos–Uzawa method with a 13th-order polynomial for the spectral element method. The computational resolution was found to be sufficient for the last mode presented for both domains, as discussed above. The condition number of the pressure matrix, S, was higher than the one in the Stokes eigen-system; approximately three times more

FIG. 8. Velocity vector plots of the first four singular Stokes eigenfunctions for the grooved channel domain; here $\|\rho(\mathbf{x})\|_\infty = 1.5$. A 13th-order Gauss Lobatto–Legendre polynomial was used in the spectral element discretization in both spatial directions. The first, second, third, and fourth eigenfunctions are plotted in (a)–(d), respectively. Velocity vector plots for eigenfunctions 10, 20, 30, 40, 50, and 60 are plotted in (e)–(j), respectively.

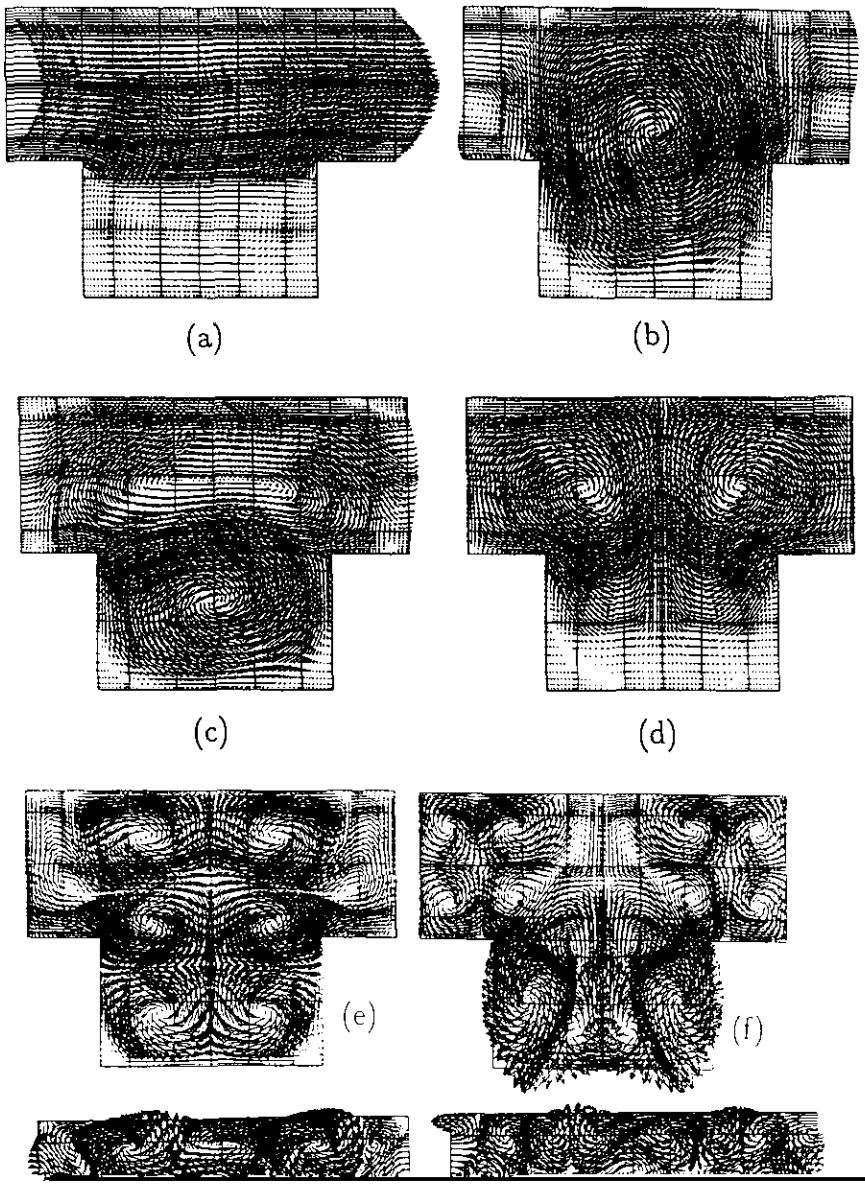
(a)
(b)
(c)
(d)
(e)
(f)

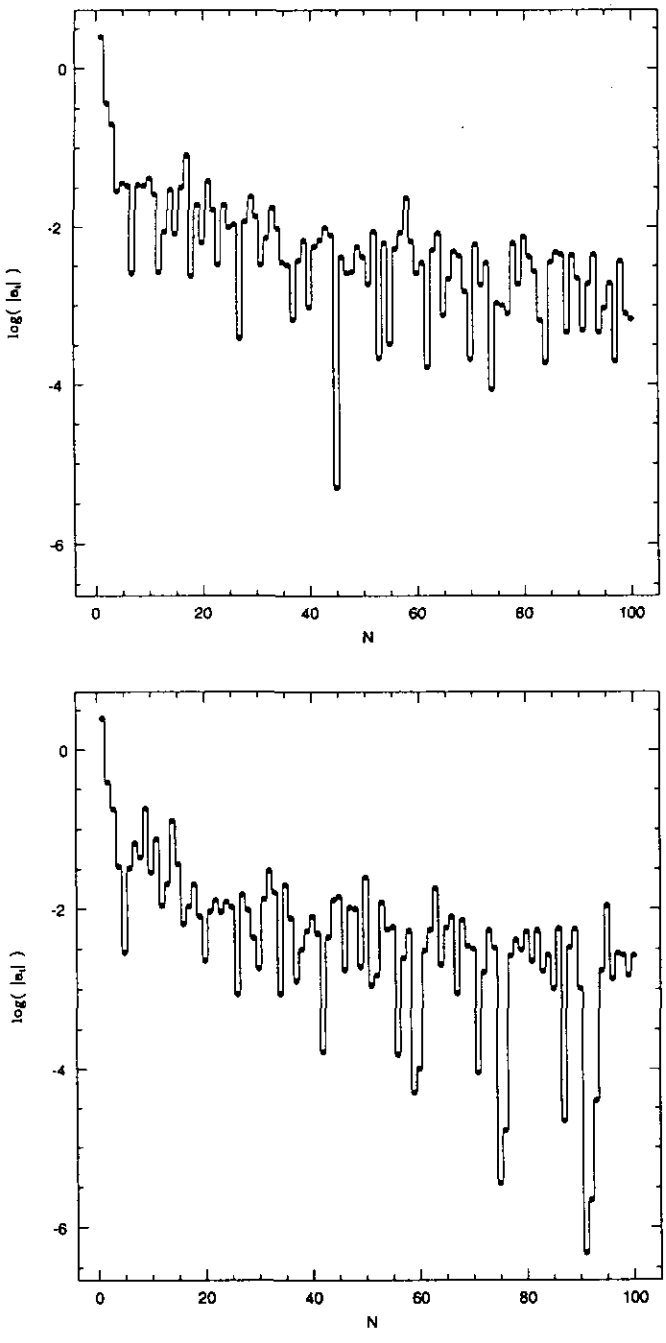

FIG. 11. Coefficients of a least squares projection for the Stokes (a) and singular Stokes (b) eigenfunctions based on the Navier–Stokes flow ($R = 100$) spectral element solution in the grooved channel ($\|\rho(\mathbf{x})\|_\infty = 2.0$).

expansions were 3.4×10^{-3} and 1.2×10^{-2} for the Stokes and singular Stokes eigenfunction projections, respectively.

For both $R = 100$ and 350 the L^2 error norm decays at roughly the same rate with slight differences in the magnitude, slightly less than 0.5% maximum pointwise error for a 100 mode projection. There are noticeable differences in the decay rates of the coefficients. The singular Stokes system demonstrates rapid decay of selected coefficients which is expected from the discussions presented in Section 4.1, see Fig. 11. At this point, no conclusive statement can be made on either expansion other than that the magnitude of the L^2 error norm is $O(10^{-3})$ after 100 modes for both sets. Different $\|\rho(\mathbf{x})\|_\infty$ had little effect on the error norms of the projections. The value $\|\rho(\mathbf{x})\|_\infty = 1.5$ gave the lowest error norm for the singular systems defined above; however, it did not produce significantly better results than the Stokes eigen-system projection.

Eddy-Promoter Results. The L^2 level of divergence for an accurate spectral element simulation of the Navier–Stokes equations was 2.5×10^{-6} for the $R = 100$ solution and 2.8×10^{-6} for the $R = 350$ solution for the 54 element eddy-promoter domain. The solution at $R = 350$ is unsteady, whereas the $R = 100$ is a stationary solution. The L^2 error norm and the coefficients for the L^2 projections of the $R = 100$ simulation onto the Stokes and singular Stokes sets, $\|\rho(\mathbf{x})\|_\infty = 1.3$, follow a similar decay rate as that of the grooved channel; see [12]. The divergence levels for the 150 mode expansions were 3.4×10^{-5} and 4.7×10^{-5} for the Stokes and singular Stokes eigenfunction projections, respectively.

Again the $R = 350$ projection has similar qualitative results as that of the $R = 100$ case for both the convergence of the L^2 error norm and decay of the projection coefficients. Reconstructions with 100 modes for the Stokes and singular Stokes systems results in approximate solutions within 10^{-3} of the spectral element solution. The divergence levels for the 100 mode expansions were 5.4×10^{-5} and 4.8×10^{-4} for the Stokes and singular Stokes eigenfunction projections, respectively.

7. GALERKIN PROJECTIONS OF THE NAVIER–STOKES EQUATIONS

7.1. Formulation

The governing equations for Newtonian fluids are the incompressible Navier–Stokes equations written in conservative form as

$$\frac{\partial \mathbf{v}}{\partial t} + \nabla \cdot (\mathbf{vv}) = -\nabla p + \nu \nabla^2 \mathbf{v} + \mathbf{f} \qquad \text{in } \Omega \qquad (17a)$$

$$\nabla \cdot \mathbf{v} = 0 \qquad \text{in } \Omega, \qquad (17b)$$

where $\mathbf{v}$ is the velocity field ($\mathbf{v}(\mathbf{x}, t)$), p is the static pressure, $\mathbf{f}$ is a given external body force, ν is the kinematic viscosity of the fluid. The solution of the above system is found by a Galerkin projection subject to mixed homogeneous periodic boundary conditions. A trial basis $\{\mathbf{w}_i(\mathbf{x})\}$ and a set of test functions $\{\mathbf{\Phi}_i(\mathbf{x})\}$ are defined which are solenoidal (therefore satisfying the incompressibility constraint) and satisfy

the boundary conditions. These sets define the projection and are chosen to be the same as the trial basis due to the orthogonality of the eigen-systems. The solution is expanded in terms of the trial basis, $\mathbf{v}(\mathbf{x}, t) = \sum_{i=0}^{N} a_i(t)\, \mathbf{w}_i(\mathbf{x})$, and the time dependent expansion coefficients are solved for. The governing equations are projected onto the set of test functions and the pressure is eliminated.

To deal with non-homogeneous boundary conditions a boundary function, Ψ, is assumed to exist, which can be readily computed by solving the steady state Stokes equations, subject to the appropriate boundary conditions:

$$-\nabla\Gamma + \nabla^2\Psi = 0 \qquad \text{in } \Omega \tag{18a}$$

$$\nabla \cdot \Psi = 0 \qquad \text{in } \Omega \tag{18b}$$

$$\mathscr{B}\Psi = \mathscr{B}\mathbf{v} \qquad \text{on } \partial\Omega. \tag{18c}$$

The boundary function is divergence-free by construction and is subtraced from the actual solution. The difference between the velocity field and the boundary function, $\mathbf{u} = \mathbf{v} - \Psi$, is then solved for. This field is subject to new forcing terms and the boundary conditions are homogeneous or periodic,

$$\frac{\partial \mathbf{u}}{\partial t} + \mathbf{u} \cdot \nabla \mathbf{u} = -\nabla p + \nu \nabla^2 \mathbf{u} - \mathbf{F} \qquad \text{in } \Omega \tag{19a}$$

$$\nabla \cdot \mathbf{u} = 0 \qquad \text{in } \Omega \tag{19b}$$

$$\mathscr{B}\mathbf{u} = 0 \qquad \text{on } \partial\Omega, \tag{19c}$$

where $\mathbf{F} = \mathbf{u} \cdot \nabla\Psi + \Psi \cdot \nabla\mathbf{u} + \Psi \cdot \nabla\Psi - \mathbf{f}$.

7.1.1. *Projections and Expansions*

Weak solutions of the Navier–Stokes equations, $\Omega \subset \Re^d$, are obtained from

$$\frac{d(\mathbf{v}, \boldsymbol{\Phi})}{dt} + \nu(\nabla\mathbf{v}, \nabla\boldsymbol{\Phi}) + (\nabla \cdot (\mathbf{vv}), \boldsymbol{\Phi}) = (\mathbf{f}, \boldsymbol{\Phi}) \qquad \forall \boldsymbol{\Phi} \in H_0^1 \tag{20}$$

for $A^{-1/2}\mathbf{f} \in H$, where

$$H = \{\mathbf{u} \in L^2(\Omega) \mid \nabla \cdot \mathbf{v} = 0\}$$

$$H_0^1 = \{\nabla\mathbf{v} \in L^2(\Omega) \mid \nabla \cdot \mathbf{v} = 0,\ \mathscr{B}\mathbf{v} = 0 \text{ on } \partial\Omega\}$$

$$A\colon \mathscr{D}(A) \subset H \to H, \qquad A = -P\nabla^2,$$

and P is the orthogonal projection $P\colon L^2(\Omega^d) \to H$. Periodic boundary conditions are also contained in H_0^1 and solutions are obtained by expanding the solution in terms of the trial basis,

$$\mathbf{v}_N(\mathbf{x}, t) = a_i(t)\, \mathbf{w}_i(\mathbf{x}), \qquad i = 1, 2, 3, \ldots, N, \tag{21}$$

where $\{\mathbf{w}_i(\mathbf{x})\}$ and $\{\boldsymbol{\Phi}_i(\mathbf{x})\}$ are complete in H_0^1. By taking the inner product of the governing equations with the test functions we obtain a nonlinear system of ordinary differential equations for the time dependent coefficients of the expansion. The use of solenoidal test functions removes the pressure from the system through Green's identity,

$$\int_\Omega \boldsymbol{\Phi}_i \cdot \nabla p = \int_\Omega (\nabla \cdot \boldsymbol{\Phi}_i)\, p - \int_{\partial\Omega} p(\mathbf{n} \cdot \boldsymbol{\Phi}_i). \tag{22}$$

The system of N ordinary differential equations found by retaining a N-term Galerkin projection is

$$\frac{da_i}{dt} = c^1_{i,j} a_j - c^2_{i,j,k} a_j a_k - \nu c^3_{i,j} a_j + f_i + \sigma_i, \tag{23}$$

where

$$c^1_{i,j} = (\mathbf{w}_i, \nabla \cdot (\Psi\mathbf{w}_j)) + (\mathbf{w}_i, \nabla \cdot (\mathbf{w}_j\Psi)) \tag{24a}$$

$$c^2_{i,j,k} = (\mathbf{w}_i, \nabla \cdot (\mathbf{w}_k\mathbf{w}_j)) \tag{24b}$$

$$c^3_{i,j} = (\nabla\mathbf{w}_i, \nabla\mathbf{w}_j) \tag{24c}$$

$$f_i = (\mathbf{w}_i, \mathbf{f}) \tag{24d}$$

$$\sigma_i = (\mathbf{w}_i, \Psi \cdot \nabla\Psi). \tag{24e}$$

In the case of $d = 2$ the existence of solutions has been proven, and for the $d = 3$ case the existence is known only for finite time intervals [22]. In this study only solutions in two-dimensional domains shown in Fig. 1 are considered.

This system can be solved by various solution methods for ordinary differential equations. Here, the second-order Crank–Nicolson method is employed for the linear operator and a third-order Adams–Bashforth integration is used to evaluate contributions from the quadratic non-linearity.

7.1.2. *Treatment of the Nonlinear and Diffusion Terms*

The treatment of the nonlinear term was found to be of critical importance when projections are performed with modes of small but measurable divergence errors, i.e., of order 10^{-3} in L^2. The conservation form $\nabla \cdot (\mathbf{vv})$ was found to yield significantly more accurate results than the rotational form $\mathbf{v} \times (\nabla \times \mathbf{v})$. The computed eigenfunctions are calculated on a piecewise p-order polynomial mesh and therefore the projections of the nonlinear term, Eq. (24b), requires the integration of a $(3p-1)$-degree polynomial. This can be obtained accurately with a $\frac{3}{2}p$-order Gaussian quadrature. The projection coefficients for the nonlinear term have been calculated on a $\frac{3}{2}p$-order Gauss mesh and differences of the order of 10^{-8} were found with respect to the p-order Gauss Lobatto mesh for all 150^3 coefficients in the 88-element eddy-promoter domain; similar results were obtained for the 58-element grooved channel domain. Based

on this result and the added cost of the interpolation for the $\frac{3}{2}p$ mesh all projection coefficients were computed on the p-order Gauss Lobatto mesh for the Navier–Stokes simulations presented in Section 7.

Computation of the projection coefficients for the non-linear term is responsible for the largest percentage of pre-processing time. There are N^3 coefficients which must be computed and stored in advance. The computational complexity of evaluating the non-linear projection coefficients can be significantly reduced by integrating by parts and arriving at

$$c^2_{i,j,k} = (\mathbf{w}_i, \nabla \cdot (\mathbf{w}_k \mathbf{w}_j)) = -(\nabla \mathbf{w}_i, (\mathbf{w}_k \mathbf{w}_j)). \tag{25}$$

Evaluation of the non-linear coefficients is therefore reduced to one computation of the gradient for each eigenfunction and a series of inner product operations. A further reduction in work can be found by making use of known symmetries of the coefficients. By defining a trilinear form

$$b(\mathbf{u}, \mathbf{v}, \mathbf{w}) = \int_\Omega u_j \frac{\partial v_i}{\partial x_j} w_i \, d\mathbf{x}, \tag{26}$$

where the subscripts indicate vector index notation, and noting that the vectors are divergence-free and have homogeneous or periodic boundary conditions, we find that

$$b(\mathbf{u}, \mathbf{v}, \mathbf{w}) = -b(\mathbf{u}, \mathbf{w}, \mathbf{v}) \tag{27a}$$

$$b(\mathbf{u}, \mathbf{v}, \mathbf{v}) = 0. \tag{27b}$$

In terms of the notation for the projection coefficients presented above we find that

$$c^2_{i,j,k} = -c^2_{j,i,k} \tag{28a}$$

$$c^2_{i,i,k} = 0. \tag{28b}$$

The total computational work required is N vector gradient evaluations and $\frac{1}{2}(N^3 - N^2)$ inner product evaluations. The storage requirements are $\frac{1}{2}(N^3 - N^2)$ as well.

Simplification procedures are also used to evaluate the projection of the Laplacian by noting that

$$c^3_{i,j} = (\nabla \mathbf{w}_i, \nabla \mathbf{w}_j) = \mathbf{w}_i^{\mathrm{T}} \mathbf{A} \mathbf{w}_j, \tag{29}$$

where $\mathbf{A}$ is the discrete Laplacian of the spectral element discretization. Noting the symmetry of the $c^3_{i,j}$ coefficients, we find a total computational work of N matrix vector multiplications $\mathbf{A}\mathbf{w}_j$, where efficient sum factorization techniques can be employed [7] and $\frac{1}{2}(N^2 + N)$ inner product evaluations. The storage requirements are $\frac{1}{2}(N^2 + N)$ as well.

7.2. Stokes Flow Solutions

In this section the results of Galerkin solutions of the Stokes equations are presented, Eq. (17a), where $\partial/\partial t' = 0$, $\mathbf{v} \cdot \nabla \mathbf{v} = 0$, and $\nu = 1$. For the Stokes equations the system of ordinary differential equations, Eq. (23), reduces to

$$c^3_{i,j} a_j = f_i, \tag{30}$$

where the boundary conditions for the grooved channel and eddy-promoter domains are the no-slip conditions at the rigid walls and periodicity at the inlet and outlet of the channel regions. The eigenfunctions satisfy the imposed boundary conditions and therefore Ψ is not pesent in the formulation.

A Stokes flow was computed by the spectral element method described in Section 2.2, where the forcing was chosen to be a constant in the x-direction, $\mathbf{f} = (C_x, 0)$. This solution is considered to be an accurate solution so that error norms based on it are presented. Convergence of the L^2 error norm comparing the Stokes and singular Stokes Galerkin solutions to the spectral element solution are presented in Fig. 12 for the grooved channel domain. The L^2 divergence level of the spectral element solution is 4.1×10^{-4}, the solution with 100 Stokes eigenfunctions is 3.9×10^{-4}, and the solution with 100 singular Stokes eigenfunctions is 1.0×10^{-3}. For the eddy-promoter domain the convergence of the L^2 error norm comparing the Stokes and

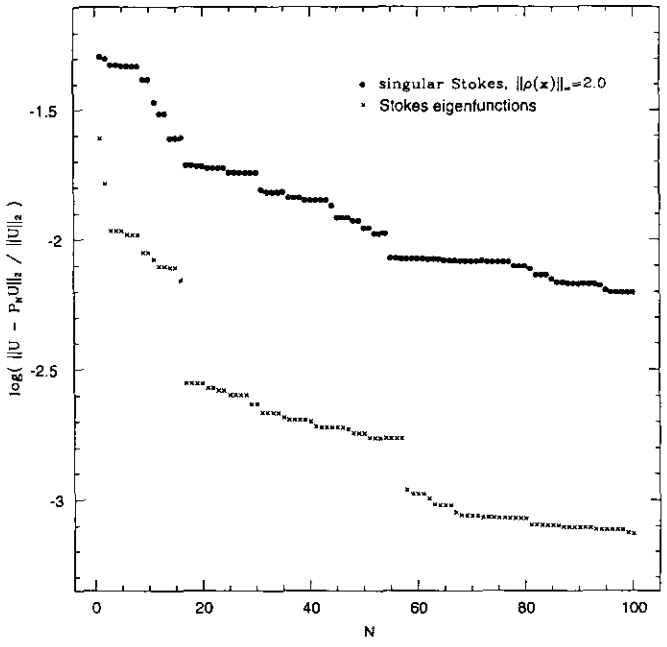

FIG. 12. Convergence of the Galerkin solution of the Stokes equations with the use of the Stokes and singular Stokes eigenfunctions for the grooved channel domain are plotted here ($\|\rho(\mathbf{x})\|_\infty = 2.0$). The L^2 error norm with respect to the Stokes flow computed by the spectral element method is plotted.

singular Stokes Galerkin solutions to the spectral element solution slightly less than those for the grooved channel with the same trends. The L^2 divergence level of the spectral element solution is 1.4×10^{-7} for the 88-element mesh, the solution with 150 Stokes eigenfunctions is 1.4×10^{-7}, and the solution with 150 singular Stokes eigenfunctions is 7.5×10^{-6}. For more details see [12].

7.3. Navier–Stokes Solutions

7.3.1. *Stationary Solutions*

The time independent weak solutions of the Navier–Stokes equations are considered,

$$\nu(\nabla \mathbf{v}, \nabla \boldsymbol{\Phi}) + (\nabla \cdot (\mathbf{vv}), \boldsymbol{\Phi}) = (\mathbf{f}, \boldsymbol{\Phi}) \qquad \forall \boldsymbol{\Phi} \in H_0^1 \qquad (31)$$

for $A^{-1/2}\mathbf{f} \in H$. Solutions are presented for various Reynolds numbers for the grooved channel and eddy-promoter domains. Results are presented for the Stokes and singular Stokes eigen-systems described above and the distribution of the energy spectrum, a_i^2, for the various solutions are presented. The solutions are obtained by a Newton–Raphson iteration and by Eq. (23) until steady state solutions are obtained.

Grooved Channel Results. The convergence in the L^2 error norm for the Stokes and singular Stokes, $\|\rho(\mathbf{x})\|_\infty = 2.0$, eigen-systems when compared to the spectral element simulation at $R = 100$ is presented in Fig. 13. The singular Stokes system gives a fairly consistent decay while the Stokes system tends to produce large fluctuations in the error norm as the dimension of the system is increased. The magnitude of the L^2 error norm is approximately the same for both systems for an expansion of 100 modes.

In Figs. 14a and 14b the profiles of the streamwise com-

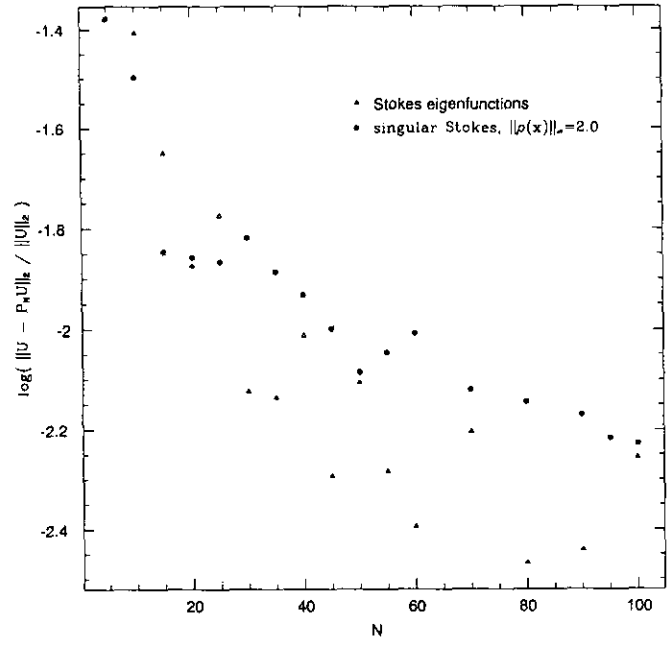

FIG. 13. Convergence of the Galerkin solution of the Navier–Stokes equations at $R = 100$ for the Stokes and singular Stokes eigenfunctions in the grooved channel domain ($\|\rho(\mathbf{x})\|_\infty = 2.0$). The L^2 error norm with respect to the Navier–Stokes flow computed by the spectral element method is plotted here.

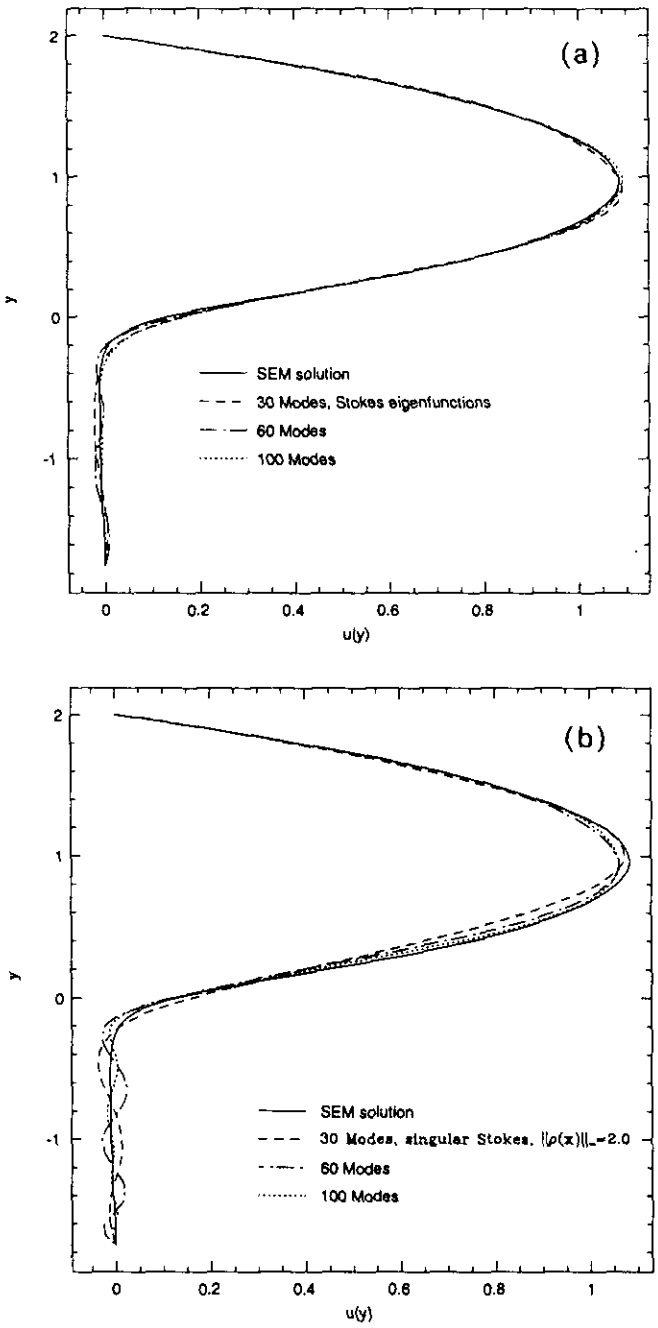

FIG. 14. Streamwise velocity profile at $x = 1.3$, slightly downstream of the $3\pi/2$ corner nearest the inlet. The Galerkin solutions with the Stokes (a) and singular Stokes (b) eigen-systems are presented and compared to the spectral element solution (SEM) for the grooved channel.

ponent of velocity are plotted at a x-location of 1.3 (just after the $3\pi/2$ corner nearest the inlet) for the Stokes and singular Stokes systems. The plots show the convergence to the spectral element solution for both basis sets for expansions of 30, 60, and 100 modes. The profile depicts a steep gradient at the location of the shear layer following the corner. Both basis sets appear to capture the profile shape accurately to within an error of about 1% with the Stokes system giving the better results. In Fig. 15 the profiles of the vertical component of velocity at the x-locations of 1.3 and 3.1 (approximately at the core of the recirculation zone in the groove region) for a 100-mode Galerkin solution are plotted. The Stokes eigen-system gives a poor approximation to the qualitative shape of the profile while the singular Stokes system converges to a profile in good qualitative agreement with the spectral element simulation. The ability of the singular system to capture both components of velocity is an interesting feature and illustrates the robustness of the eigenfunctions of singular operators to capture complicated profiles with relatively low dimensional expansions. The coefficients of the Galerkin solution of the Navier–Stokes equations for the $R = 100$ case are similar to those presented in Section 6; however, here the singular system gives rapid decay of selected coefficients while the Stokes system exhibits a nearly flat distribution of energy for the higher modes.

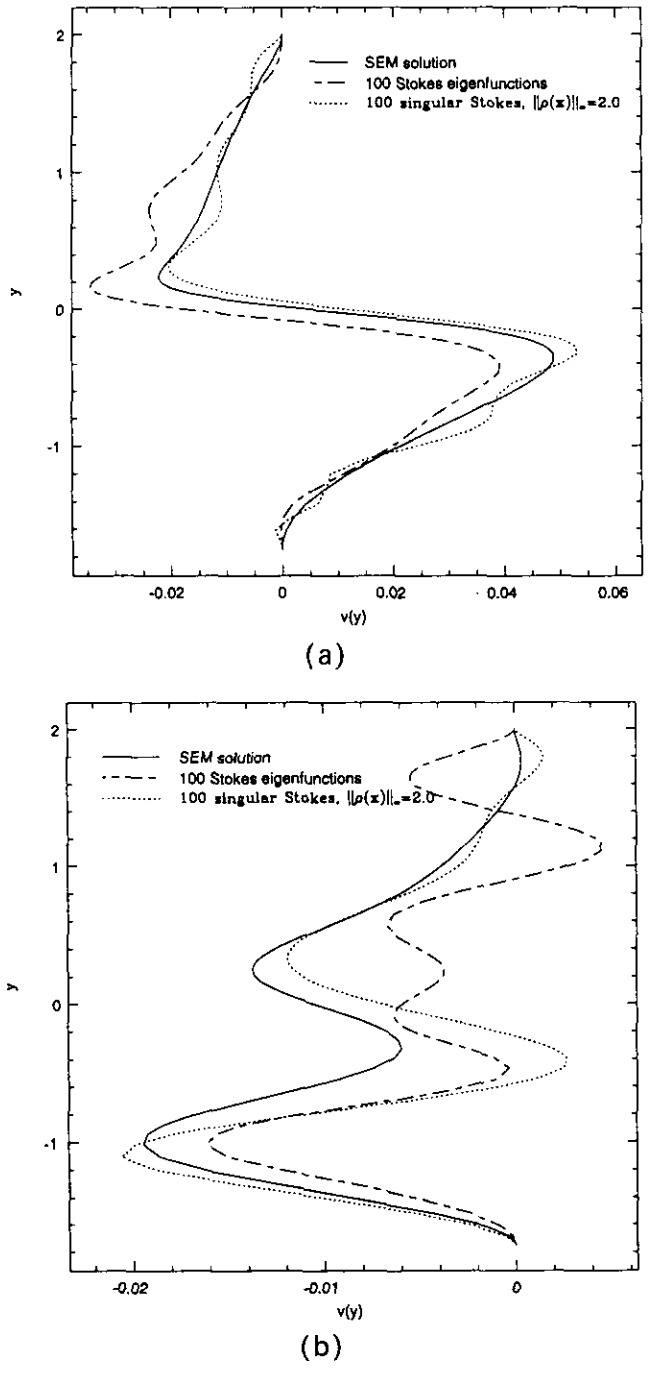

FIG. 15. Vertical velocity profile for the $R = 100$ solution in the grooved channel: (a) $x = 1.3$ (slightly downstream of the $3\pi/2$ corner nearest the inlet); (b) $x = 3.1$ (approximately at the core of the recirculation zone in the groove). Results are presented for the 100-mode Stokes and singular Stokes Galerkin projections and the SEM.

Eddy-Promoter Results. Convergence in the L^2 error norm for the Stokes and singular Stokes eigenfunctions ($\|\rho(\mathbf{x})\|_\infty = 1.3$), when compared to the spectral element simulation at $R = 100$, is presented in Fig. 16 for 150 modes in the eddy-promoter domain. The qualitative results of the L^2 error are similar to that of the grooved channel; however, the eddy-promoter domain results in an error with a slightly

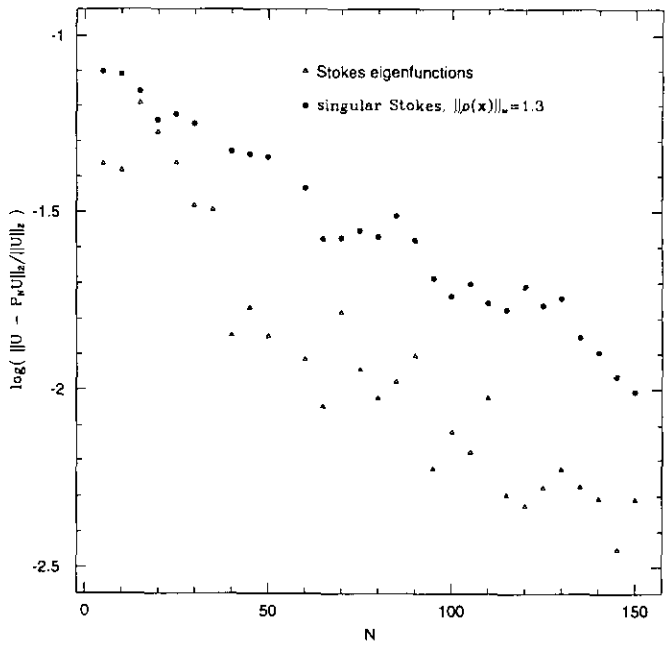

FIG. 16. Convergence of the Galerkin solution of the Navier–Stokes equations at $R = 100$ for the Stokes and singular Stokes eigenfunctions in the eddy-promoter domain ($\|\rho(\mathbf{x})\|_\infty = 1.3$). The L^2 error norm with respect to the Navier–Stokes flow computed by the SEM is plotted here.

larger magnitude. The Stokes system tends to yield a slightly lower error norm with both basis sets corresponding to approximately 1% errors.

In Figs. 17a and 17b the streamwise velocity profile is plotted at a location 0.4 units downstream of the center of the cylinder, $(x_c, y_c) = (1.5, -0.5)$, with a diameter of 0.4 units. Convergence to the accurate spectral element solution is demonstrated where the Stokes system tends to approximate the profile slightly better than the singular Stokes solution. In Figs. 18a and 18b the vertical component of the velocity profile is plotted at 0.4 units downstream of the cylinder center for selected solutions of the Stokes and singular Stokes projection. In Figs. 19a and 19b the vertical velocity profile is plotted at a $x = 4.18$ near the end of the domain of 4.283 units. Again both sets show convergence to the spectral element solution.

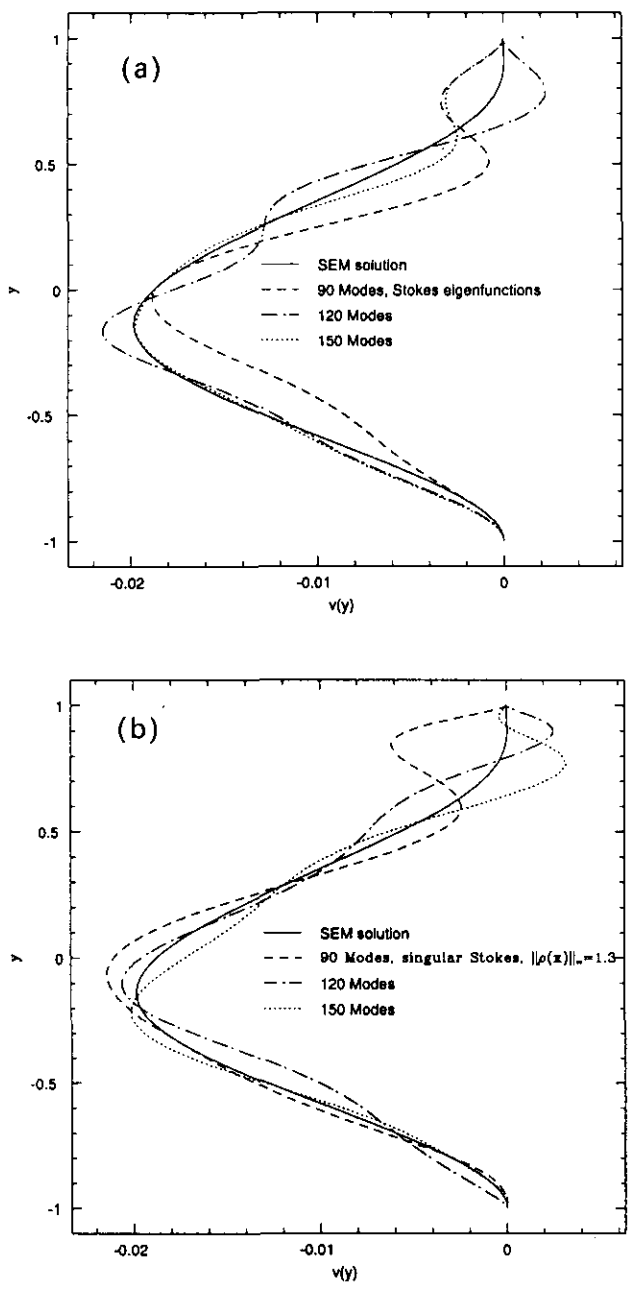

FIG. 19. Vertical velocity profile at $x = 4.18$ near the end of the domain at $x = 4.283$ for the $R = 100$ Galerkin and spectral element solutions. The Galerkin solutions for the Stokes (a) and singular Stokes (b) eigen-systems are presented and compared to the SEM for the eddy-promoter domain.

Figure 20 presents the pointswise error associated with Figs. 15a and 18 for the grooved channel and eddy-promoter domains, respectively. The singular Stokes solutions tend to cluster the zeros of the truncation error closer to the wall and the magnitude of the error is less in the near wall region relative to the Stokes eigenfunction projection. Note also the increased number of zero crossings of the singular Stokes error versus that of the Stokes error in Fig. 20. This behavior illustrates the robust character of basis sets that cluster zeros near the domain boundary, as do the eigenfunctions of singular operators. Such clustering of zeros can be linked to sets that closely minimize the L^∞ error norm in polynomial approximations to functions and is expected to generally apply to the somewhat more abstract basis sets discussed here.

7.3.2. *Unsteady Solutions*

Grooved Channel Results. The spectral element simulation of flow that is subject to a constant forcing, $\mathbf{f} = (2\nu, 0)$, in the grooved channel domain undergoes a transition to unsteady flow at a Reynolds number between 260 and 270 for a 5×5 simulation and has been reported to undergo transition at a Reynolds number of approximately 300 for a 9×9 simulation [35]. In Table III the bifurcation Reynolds number as a function of the number of modes retained for the Galerkin solution with the Stokes and singular Stokes ($\|\rho(\mathbf{x})\|_\infty = 2.0$) eigen-systems are presented. The Stokes system exhibits large fluctuations in the bifurcation point with respect to the dimension of expansion while the singular Stokes system tends to level off and approaches the spectral element solution.

In Figs. 21 and 22 selected snapshots of the unsteady $R = 350$ and 1000 simulations by the spectral element method and 95-mode Stokes and singular Stokes ($\|\rho(\mathbf{x})\|_\infty = 2.0$) eigenfunction projections are presented. The $R = 350$ solution is characterized by an oscillation of the large recirculation flow in the groove region and shedding of a smaller recirculating structure in the shear layer region just after the $3\pi/2$ corner nearest the inlet. The singular Stokes snapshot was chosen so that the core of the smaller recirculation structure was in approximately the same location as the spectral element solution snapshot. The singular Stokes solution is in good agreement with the qualitative shape of the outlet profile, large recirculation in the groove region, and the size of the smaller recirculation structure in the shear layer region. The Stokes eigenfunction solution did not resolve the small recirculation structure in the shear layer region and the qualitative agreement with the outlet profile and shape of the larger recirculation in the grooved region is less favorable; the selection of the snapshot was taken with less precision due to the noticeable error present.

The $R = 1000$ solution is characterized by a larger recirculation in the groove region, a more nonsymmetric outlet profile, and the appearance of a separation region which travels along the top wall. The singular Stokes snapshot was chosen so that the top separation region was positioned in approximately the same location as the snapshot of the spectral element solution. The singular Stokes solution gives good qualitative agreement with the outlet profile, the shape

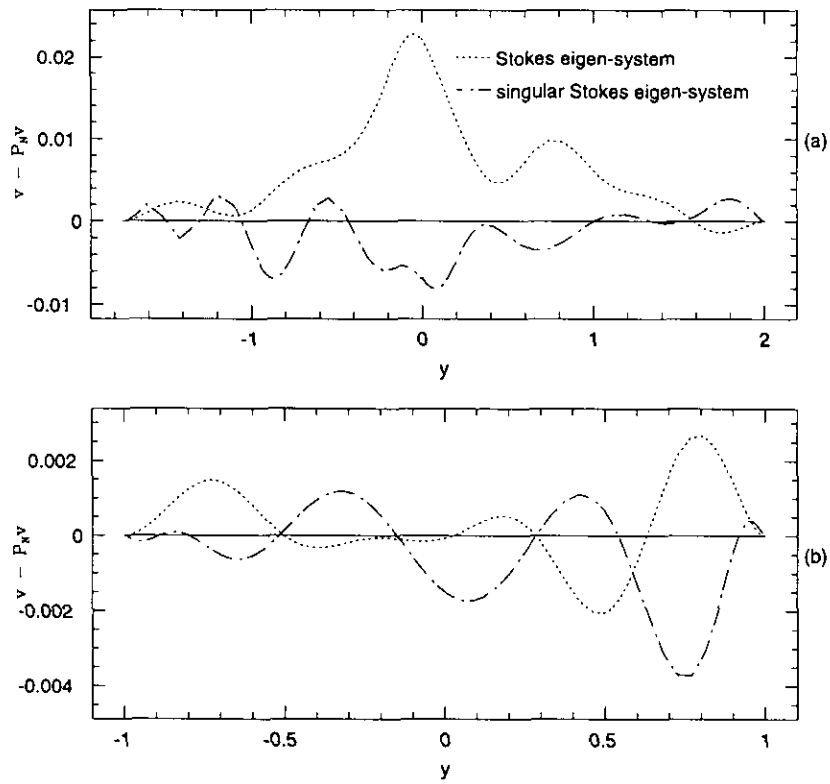

FIG. 20. The pointwise error relative to the spectral element solution for the vertical velocity profiles plotted in Figs. 15 and 18: (a) is a profile at $x = 1.3$ for a 100-mode Galerkin solution in the grooved channel ($R = 100$); (b) is a profile at $x = 1.9$ for a 150-mode projection for the eddy-promoter domain ($R = 100$).

of the large recirculation in the groove region, and the appearance of the separation region that travels along the top wall. The relative size of the error can be seen in the groove region where noticeable oscillations in the truncation error are present near the vertical wall closest to the inlet. The Stokes eigenfunction solution gives poor agreement as can be seen by the oscillations in the truncation error in the outlet profile; such oscillations are also noticeable in the $R = 350$ solution.

Time history data for the streamwise component of the velocity is plotted in Figs. 23 and 24 for the $R = 350$ and 1000 simulations, respectively, at $(x, y) = (1.063, 0.023)$ for a 95-mode Galerkin solution of the Stokes and singular Stokes eigen-systems and at $(x, y) = (1.069, 0.052)$ for a 5×5 spectral element solution. The slight change in location has negligible effect on the data and higher-order spectral element simulations tend to lower the rms value for the fluctuating component of the solution. The singular Stokes solution gives good agreement with the rms value of the fluctuating component and has less than 1% error in the frequency of the oscillation at $R = 350$. The Stokes system gives poor comparison in frequency content and rms levels of the fluctuations. The maximum velocity of the solutions is approximately one. The $R = 1000$ simulations give periodic results for the spectral element simulation and singular Stokes projection while the Stokes eigenfunction projection gave a more distorted aperiodic result. The higher harmonics tend to be more pronounced in the singular Stokes projection; this is most likely due to the larger error present with respect to the spectral element solution.

The convergence to the correct dynamical result is clearly illulstrated by a lower dimensional projection. In Fig. 25 the first coefficient time history is plotted for a 30-mode singular Stokes Galerkin solution of the Navier–Stokes equations ($R = 1000$) in the grooved channel domain. The time history indicates an erroneous chaotic signal with intermittent structure.

TABLE III

Bifurcation Reynolds Number for the Grooved Channel Domain

N	R_{cr} Stokes	R_{cr} singular Stokes
60	180–200	360–370
70	200–220	490–500
80	100–150	270–280
90	—	230–240
95	180–200	240–250
100	—	240–250

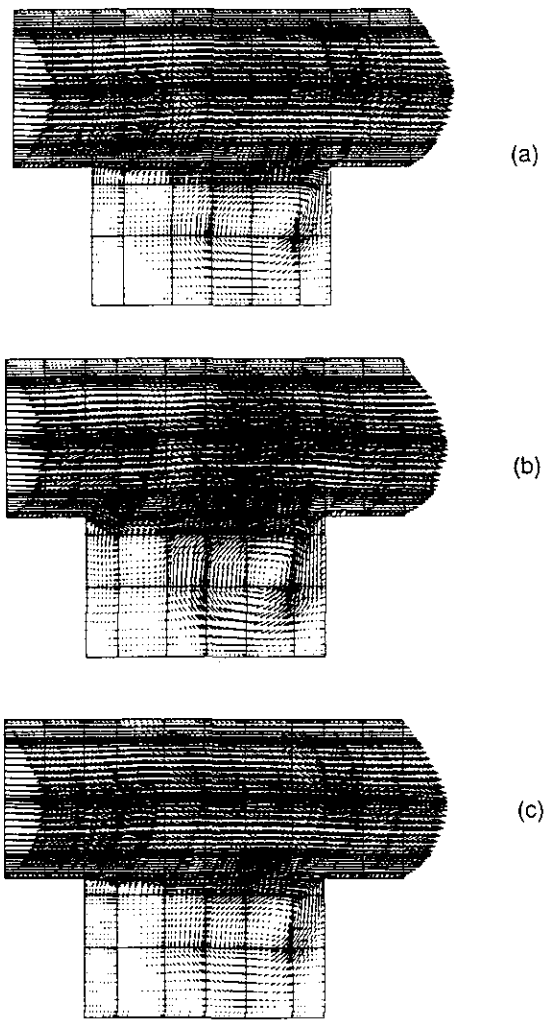

FIG. 21. Velocity vector plots for selected snapshots at $R = 350$: (a) spectral element solution; (b) 95 Stokes eigenfunctions; (c) 95 singular Stokes eigenfunctions.

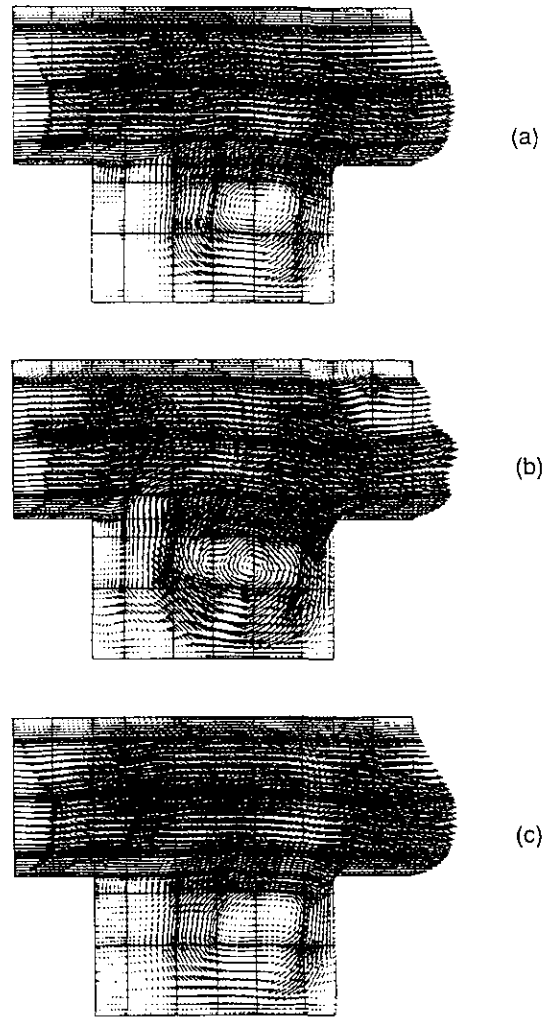

FIG. 22. Velocity vector plots for selected snapshots at $R = 1000$: (a) spectral element solution, (b) 95 Stokes eigenfunctions; (c) 95 singular Stokes eigenfunctions.

Eddy-Promoter Results. The spectral element simulations of flow subject to a constant forcing, $\mathbf{f} = (2\nu, 0)$, in the eddy-promoter domain undergoes a transition to unsteady flow at a Reynolds number between 330 and 350 for a 9×9 simulation with a 88-element mesh. In Table IV the bifurcation Reynolds number for various Galerkin solutions with the Stokes and singular Stokes ($\|\rho(\mathbf{x})\|_\infty = 1.3$) eigensystems are presented. The prediction of the bifurcation point with the Stokes eigen-system tends to fluctuate and then levels off, exhibiting slow convergence, at approximately a 100-mode projection. The predicted critical Reynolds number is significantly below the accurate spectral element solution. The singular Stokes solution shows less fluctuation in the bifurcation point and levels off to a Reynolds number much closer to the accurate solution.

In Figs. 26 and 28 selected snapshots of the unsteady $R = 450$ and 1000 simulations by the spectral element method and 150-mode Stokes and singular Stokes ($\|\rho(\mathbf{x})\|_\infty = 1.3$) eigenfunction projections are presented. The $R = 450$ solution is characterized by a separation region which travels along the floor of the domain and a modest oscillation of the near wake region of the cylinder. The singular Stokes snapshot was chosen so that the separation region along the bottom wall was positioned in approximately the same location as the spectral element solution. The singular Stokes solution captures all the qualitative features of the spectral element solution. The detailed shape of the outlet profile is in good agreement with the spectral element solution; however, there are slightly larger oscillations in the near wake of the cylinder. The

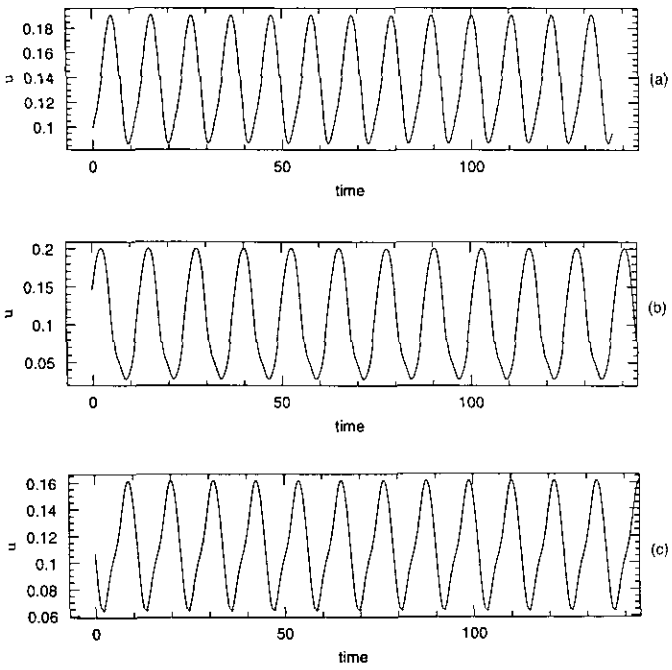

FIG. 23. Time history data near the shear layer region in the grooved channel domain for a $R = 350$. Streamwise velocity is plotted for the (a) 5×5 spectral element solution; (b) 95 Stokes eigenfunctions; (c) 95 singular Stokes eigenfunctions.

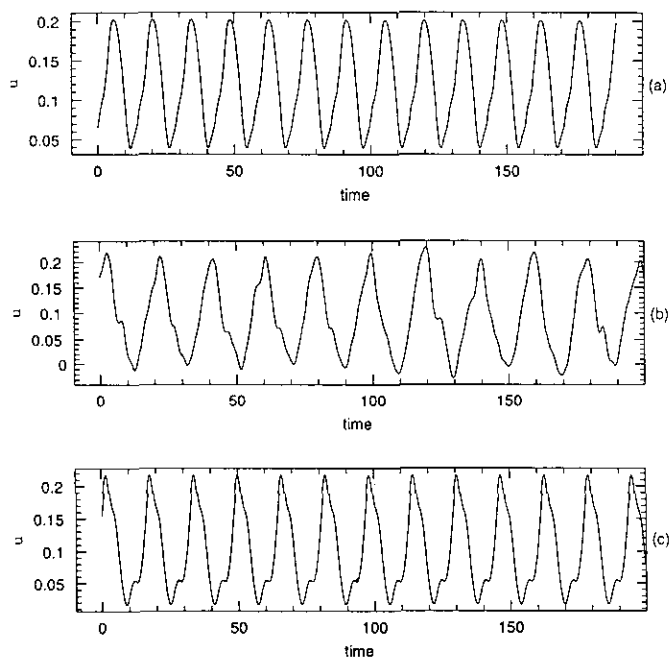

FIG. 24. Time history data near the shear layer region in the grooved channel domain for a $R = 1000$. Streamwise velocity is plotted for the (a) 5×5 spectral element solution; (b) 95 Stokes eigenfunctions; (c) 95 singular Stokes eigenfunctions.

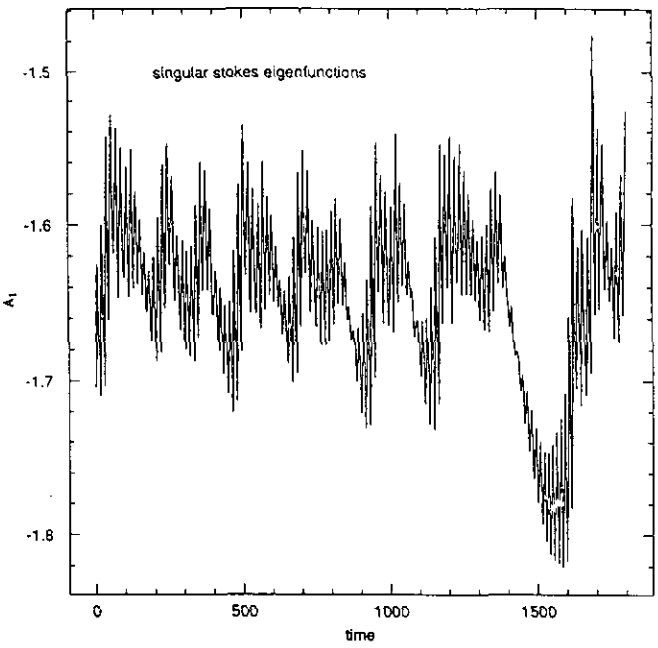

FIG. 25. Time history for the first coefficient of a 30-mode singular Stokes Galerkin solution of the Navier–Stokes equations ($R = 1000$) in the grooved channel domain.

150-mode Galerkin solution with the Stokes eigen-system gives poor qualitative agreement with the spectral element solution at both the outlet profile and near wake region of the cylinder and therefore the snapshot of the Stokes eigen-system was chosen with less care. The qualitative feature of the separation bubble traveling along the bottom wall is present. However, the oscillations in the pointwise error are large enough to be seen in the outlet profile and the width of the near wake region is significantly underestimated by the Stokes projection.

Time history data for the streamwise component of the velocity is plotted in Fig. 27 for the $R = 450$ simulations at $(x, y) = (2.198, -0.2)$ for a 150-mode Galerkin solution of the Stokes and singular Stokes eigen-systems and a 5×5 spectral element solution. A 9×9 spectral element simula-

TABLE IV

Bifurcation Reynolds Number for the Eddy-Promoter Domain

N	R_{cr} Stokes	R_{cr} singular Stokes
50	380–390	250–260
70	330–340	400–410
90	270–280	400–410
110	170–180	330–340
130	170–180	400–410
140	—	400–410
150	170–180	400–410

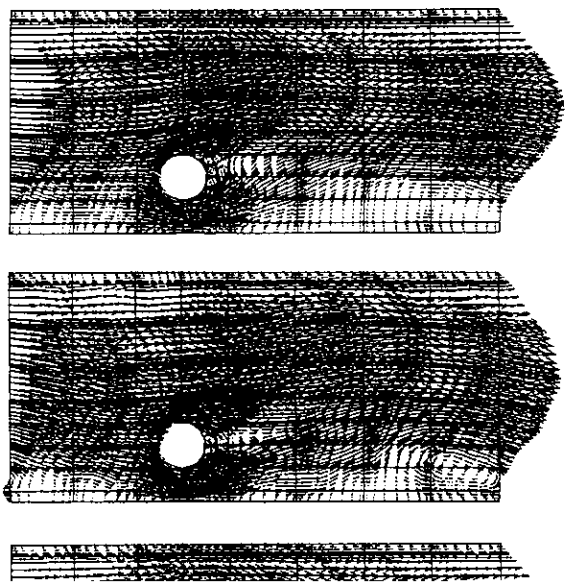

(a)

(b)

tion had only slight changes with respect to the 5×5 solution. The time history point is located 1.75 diameters behind and 0.75 diameters above the center of the cylinder. The $R = 450$ solution has a single frequency present with a period of approximately 20 time units for the spectral element solution. The Stokes and singular Stokes projections also have a single frequency present; however, the period of the oscillation is underestimated by nearly 20% by both basis sets. The amplitude of the oscillation is smaller for the singular Stokes projection. The maximum streamwise velocity for the solution is approximately one and thus the Galerkin solutions differs from the spectral element solution by approximately 10% to 15%.

The $R = 1000$ solution is characterized by a larger separation region on the lower wall of the domain and a more convoluted profile at the outlet of the domain as compared to the $R = 450$ simulation. The oscillations of the near wake region have evolved into a vortex shedding from

convoluted evolution of the outlet profile is not resolved adequately. The Stokes eigen-system solution fails to capture the vortex shedding at the top of the cylinder and the oscillations in the truncation error are again illustrated in the outlet profile, see Fig. 28c. The 150-mode Galerkin projection with the singular Stokes eigen-system has significant discrepancies with the spectral element solutions; however, the essential evolutionary characteristics of vortex shedding and bottom wall separation bubble are captured as compared to the Stokes eigen-system which fails to adequately resolve these features.

8. DISCUSSION

In this work, a new set of eigenfunctions based on a modified (singular) Stokes operator was proposed for the solution of the incompressible Navier–Stokes equations in general complex computational domains. The corresponding eigenproblem was formulated as a multi-dimensional Sturm–Liouville problem, and efficient methods for computing divergence-free, geometry-fitted vector eigenfunctions were developed. Galerkin projections, defined by these numerically obtained eigenfunctions, resulted in a simpler system of ordinary differential equations with the pressure eliminated. Several Navier–Stokes solutions were obtained for a wide Reynolds number range and for three computational domains representing simple geometries (channel flow), non-separable geometries (grooved channel flow), and multiply-connected geometries (eddy-promoter flow). Although no systematic attempt was made to exploit the fast resolution properties of the singular Stokes eigenfunctions, the accuracy in the Navier–Stokes solutions obtained was substantial. For instance, the Stokes eigensystem was shown to compute the Stokes equations subject to a constant forcing to less than 0.1% error with less than 100 degrees of freedom. The time-dependent Navier–Stokes equations were computed to less than 1% error with less than 100 degrees of freedom by employing the singular Stokes eigen-system for Reynolds numbers close to the first bifurcation to unsteady flow. For time dependent solutions the projection of Navier–Stokes equations onto a simple system of ordinary differential equations allows the use of modern techniques in the analysis of dynamical systems [36, 37]. This in turn will allow more systematic studies regarding low dimensionality of turbulent flow fields, the existence of inertial manifolds, etc. [38].

A new conclusion derived from the current study is that the Stokes eigen-system, although useful in theoretical studies, does not produce a well-suited basis set to solve the Navier–Stokes equations. The use of singular operators leads to eigenfunctions with zeros clustered at the domain boundaries. It was demonstrated that these eigenfunctions constitute a more robust basis set for the solution of the Navier–Stokes equations. The coefficient that makes the Stokes operator singular was chosen somewhat arbitrarily here. The results presented here demonstrate that higher convergence rates can be achieved if this coefficient is chosen properly. This freedom in constructing *optimal* EP operators is an obvious advantage of the methodology developed here and intelligent choices are expected to yield substantially better results than the 1% error estimates presented here; such a study is the focus of current research.

The exact definition of "What is an *optimal* EP operator?" is somewhat of an open question. A discussion of possible definitions and methods for constructing such operators is given in [12]. Clearly, the choice of the scalar $\rho(\mathbf{x})$ offers many possibilities as the only constraint is that it should vanish at the domain boundary and not change sign in the domain interior. The choice of computing $\rho(\mathbf{x})$ from an elliptic equation as adopted here is arbitrary and is based on computational convenience. For instance, an operator can be constructed which has as its first eigenfunction an approximation to a solution of the Navier–Stokes equations. The unstable stationary or time-averaged solutions of the Navier–Stokes equations could be incorporated into the first mode of the EP operator. By incorporating the most energetic scales in the first eigenmode, such as the large gradients in the near wake of the cylinder for the eddy-promoter domain, the remaining members of the basis set are not used to capture these features but rather the evolutionary character of the solution in a hierarchical manner.

A more physically-based approach in constructing an optimal operator may be developed by drawing the analogy with the methodology used in turbulence modeling, e.g., the large eddy simulation approach [39]. The singularity coefficient $\rho(\mathbf{x})$ can play the role of an eddy-viscosity appropriately normalized which vanishes at wall boundaries. The operator construction is then formulated to input the influence of the highest modes of a given expansion into a low dimensional set of the leading eigenfunctions of another operator, see [12] for a channel domain example. The use of the eigenfunctions of an EP operator with an eddy viscosity in the Laplacian would be an interesting study for high Reynolds number projections. An interesting twist on past efforts is that the Navier–Stokes equations would be solved at high Reynolds numbers, subject to a truncation error, whereas past efforts in turbulence modeling solved a governing equation which is not a Navier–Stokes equation. If such operators prove effective, then the combined use of eddy viscosity and enforcement of the first mode could be a powerful and promising tool in high Reynolds number turbulence simulations.

In summary, we have presented here a *dynamical* numerical method for computing unsteady, incompressible flows. It provides fast convergence for smooth solutions in complex computational domains. It can also produce low dimensional systems if intelligent choices of the field $\rho(\mathbf{x})$

are made or if the trial basis is enhanced appropriately with the anticipated approximate eigenstructure of the flowfield.

ACKNOWLEDGMENTS

We thank Professors I. G. Kevrekidis and S. A. Orszag for their useful suggestions regarding this work. We also thank Dr. George Lea for supporting this work under Contract ECS-9023362 of the National Science Foundation. Supplementary support was provided by AFOSR under contract F49620-94-1-0313. The computations were performed at the Pittsburgh Supercomputing Center on the C90.

REFERENCES

1. G. E. Karniadakis and S. A. Orszag, *Phys. Today*, March, 35 (1993).
2. P. Constantin, C. Foias, O. P. Manley, and R. Temam, *J. Fluid Mech.* **150**, 427 (1985).
3. D. A. Jones and E. S. Titi, *J. Math. Anal. Appl.* **168**, 72 (1992).
4. L. Kleiser and T. A. Zang, *Annu. Rev. Fluid Mech.* **23** (1991).
5. C. Canuto, M. Hussani, A. Quarteroni, and T. Zang, *Spectral Methods in Fluid Dynamics* (Springer-Verlag, New York/Berlin, 1987).
6. R. Temam, "New Emerging Methods in Numerical Analysis: Applications to Fluid Mechanics," in *Incompressible Computational Fluid Dynamics*, edited by M. D. Gunzburger and R. A. Nicolaides (Cambridge Univ. Press, Cambridge, 1993).
7. D. Gottlieb and S. A. Orszag, *Numerical Analysis of Spectral Methods: Theory and Applications* (SIAM, Philadelphia, 1977).
8. A. T. Patera, *J. Comput. Phys.* **54**, 468 (1984).
9. G. E. Karniadakis, *Appl. Numer. Math.* **6**, 85 (1989).
10. D. Funaro, A. Quarteroni, and P. Zanolli, Technical Report 530, Instituto di Analisi Numerica del Consiglio Nazionale delle Ricerche, Pavia, 1985 (unpublished).
11. C. L. Street and M. G. Macaraeg, *Appl. Numer. Math.* **6**, 123 (1989).
12. P. F. Batcho, Ph.D. thesis, Princeton University, 1993 (unpublished).
13. M. D. Gunzburger and R. A. Nicolaides, *Incompressible Computational Fluid Dynamics* (Cambridge Univ. Press, Cambridge, 1993).
14. L. Sirovich, *Q. Appl. Math.* **45**, 561 (1987).
15. G. Berkooz, P. Holmes, and J. L. Lumley, *Annu. Rev. Fluid Mech.* **25**, 539 (1993).
16. A. Leonard and A. Wray, in *Proceedings, International Conference on Numericals in Fluid Dynamics, 8th, Aachen*, Lecture Notes in Physics, Vol. 170, edited by E. Krause (Springer-Verlag, New York, 1982), p. 335.
17. E. M. Rønquist, Ph. D. thesis, Massachusetts Institute of Technology, 1988 (unpublished).
18. R. Courant and D. Hilbert, *Methods of Mathematical Physics, Vol. I* (Wiley, New York, 1937).
19. K. Yosida, *Lectures on Differential and Integral Equations* (Dover, New York; Interscience, New York, 1960).
20. H. Sagan, *Boundary and Eigenvalue Problems in Mathematical Physics* (Dover, New York, 1961).
21. G. Mètivier, *J. Math Pures Appl.* **57** (1978).
22. P. Constantin and C. Foias, *Navier–Stokes Equations*, Chicago Lectures in Mathematics (Univ. of Chicago Press, Chicago, 1988).
23. L. Gårding, "Eigenfunction Expansions," in *Partial Differential Equations*, Lectures in Applied Mathematics, Vol. 3A, edited by L. Bers, J. Fritz, and M. Schechter (Am. Math. Soc., Providence, RI, 1964), p. 303.
24. H. Strauss, *Partial Differential Equations; An Introduction* (Wiley, New York, 1992).
25. Y. Maday and A. T. Patera, *State of the Art Surveys in Computational Mechanics*, edited by A. Noor (Am. Soc. Mech. Eng., New York, 1987).
26. C. Bernadi, Y. Maday, and B. Métivet, *Numer. Math.* **51**, 655 (1987).
27. K. A. Cliffe, T. J. Garrat, and A. Spence, MAFLEP VII, edited by J. Whiteman, (1991).
28. B. L. Parlett, *The Symmetric Eigenvalue Problem* (Prentice Hall, Englewood Cliffs, NJ, 1980).
29. C. Foias, O. Manley, and L. Sirovich, *Phys. Fluids A* **2** (3) (1990).
30. C. Foias, O. P. Manley, R. Temam, and Y. M. Treve, *Physica D* **9**, 157 (1983).
31. H. Salwen, F. W. Cotton, and C. E. Grosch, *J. Fluid Mech.* **98**, 273 (1980).
32. M. Hajmirzaahmad and A. M. Krall, Singular second order operators: The maximal and minimal operators, and self-adjoint operators in between, *SIAM Rev.* **34** (4), 614 (1992).
33. W. E. Arnoldi, *Quart. Appl. Math.* **9** (1), 17 (1951).
34. G. E. Karniadakis, M. Israeli, and S. A. Orszag, *J. Comput. Phys.* **97**, 414 (1991).
35. A. E. Deane, I. G. Keverkidis, G. E. Karniadakis, and S. A. Orszag, *Phys. Fluids A* **3** (10), (1991).
36. R. Temam, *Proc. R. Soc. London A* **434**, 23 (1991).
37. M. S. Jolly, *Physica D* **63**, 8 (1993).
38. M. S. Jolly, I. G. Kevrekidis, and E. S. Titi, *Physica D* **44**, 38 (1990).
39. B. Galperin and S. A. Orszag, *Large Eddy Simulation of Complex Engineering and Geophysical Flows* (Cambridge Univ. Press, Cambridge, 1993).